Title
Structure and Function of Fungal Polysaccharide Monooxygenases

Author
Span, Elise Arielle

Publication Date
2018

Peer reviewed|Thesis/dissertation

Structure and Mechanism of Fungal Polysaccharide Monooxygenases

By

Elise Arielle Span

A dissertation submitted in partial satisfaction of the

requirements for the degree of

Doctor of Philosophy

in

Biophysics

in the

Graduate Division

of the

University of California, Berkeley

Committee in charge:

Professor Michael A. Marletta, Chair
Professor N. Louise Glass
Professor Judith Klinman
Professor Jamie H. D. Cate

Spring 2018

Structure and Mechanism of Fungal Polysaccharide Monooxygenases

by Elise Arielle Span

ABSTRACT

Structure and Mechanism of Fungal Polysaccharide Monooxygenases

by

Elise Arielle Span

Doctor of Philosophy of Biophysics

University of California, Berkeley

Professor Michael A. Marletta, Chair

Polysaccharide monooxygenases (PMOs) are a newly discovered and growing superfamily of secreted copper catalysts found in nature. Initial PMO discoveries were made in 2011 describing the role of these enzymes in the cellulolytic machinery of fungi. Since then, additional families predominantly from fungi and bacteria have been characterized as having oxidative activity towards a variety of polysaccharide substrates. Chapter 1 introduces these enzymes and describes their origins, structure, function, as well as what can be surmised about their mechanism.

Chapter 2 describes a study that probes PMO mechanism in a system utilizing insoluble (and non-quantifiable) cellulose as a substrate. A combination of *in vitro* assays and electron paramagnetic resonance studies of a panel of single amino acid variants illustrates the function of the secondary coordination sphere in O_2 activation by a cellulose-active PMO. This study bears directly on the recent controversy over the co-substrate of PMOs: although under some conditions PMOs can utilize peroxide, there is clearly a pathway for O_2 utilization.

An example of discoveries that are on the horizon in the PMO field is described in Chapter 3. Genetic experiments and biochemical characterization of a homologously expressed PMO from *Neurospora crassa* shed light on a new family of PMOs that represents a significant departure from those studied previously. These enzymes are necessary for hyphal homing and fusion in filamentous fungi.

DEDICATION

For Erv Span

TABLE OF CONTENTS

LIST OF FIGURES

LIST OF TABLES

ACKNOWLEDGMENTS

Completing a Ph.D. is by no means a fast or straightforward process. I am incredibly grateful to my advisor, Michael Marletta, along with my labmates, committee members, and collaborators for being witness to mine. Their scientific advice has been invaluable to much of what follows. I have learned a tremendous amount from Michael especially; simply observing his approach to scientific problems has imparted a true clarity into my own. I am so thankful to have had his support and a place in the laboratory, first at Scripps and then at Berkeley. Judith Klinman and Louise Glass have been especially perceptive and influential as committee members, and I am deeply grateful to them both.

I am also grateful to my former advisors, Dan Sem and Martin St. Maurice, for providing my initial opportunities in science and for teaching me much of what I know about the chemistry of life. I would not have engaged in academics as enthusiastically without the many brilliant-minded and kind-hearted teachers I have met along the way—there are too many to name here, but I want to specially thank Melissa Shew, who taught the best class I have ever taken and continues to inspire me as a friend.

I probably would not have chosen to immerse myself in doctoral study without my family, April and Erv, who instilled in me values of hard work and education and, from a young age, generously provided an environment for me to read and undertake all kinds of creative projects. My mom April put a tremendous amount of effort into raising me, and I will always be grateful for her loving attempts to understand the nature of the work I do now. I proudly took my grandfather Erv's surname, Span, a few months before my beginning graduate school and his passing, events that occurred simultaneously. I dedicate this dissertation and all I have learned during school to him.

I have always felt at home in Berkeley, due in no small part to the quality of the people who are my peers. My colleagues at UC-Berkeley quickly became dear friends who provided vital reality checks as I completed the Ph.D. All my love to Jasmine, Lindsey, Charlotte, Kendra, Dan, Eric, and the rest of you.

There are many others I would like to thank for their influence on me during graduate school. My music and meditation communities, for lessons in perspective. Friends who showed me real courage—specifically Julie and Hannah. Brian, for being a much-needed catalyst and dear friend. Miles, for guidance and laughter. Laura, for always reminding me of my light.

And the truest companions, Tansy and Henry.

CHAPTER 1: INTRODUCTION

Polysaccharide monooxygenases, or PMOs, are copper-dependent enzymes that utilize molecular oxygen to cleave glycosidic bonds. In recent years, they have been discovered as secreted enzymes in fungi and bacteria, where they are used in the conversion of polymeric carbohydrates to monomeric sugars utilizable as a carbon source. More recently, PMOs have been implicated in the infection cycles of microbial pathogens and viruses, suggesting an array of biological functions. Biochemical and genetic studies have informed on the activities and functions of these enzymes; spectroscopic and computational investigations have provided insight into the properties of the copper center and proposed reaction mechanisms. Nevertheless, it has been the role of structural studies, particularly early PMO structural studies, to uncover the novelty of this enzyme family.

Early PMO structures[1–3], even those with a non-functional metal bound, exposed an unexpected framework for catalysis—a flat active site tendered by various loops spread from a compact and rigid *beta* core. These structures and subsequent ones with the functional copper in place[4] implied a new activity, that of oxidative polysaccharide depolymerization. Continued structural study of fungal and bacterial PMOs[5–11] provided important foundations for probing function and mechanism in these "early" families. With the latest structural appearances of PMOs with novel substrates or origins[12–14], and perhaps biological functions[15], the landscape of PMO action is diversifying, and there is much on the horizon.

A superfamily of PMOs

PMOs were first classified into glycoside hydrolase family 61 (GH61) and carbohydrate-binding module family 33 (CBM33), for fungal (cellulose-active) and bacterial (chitin-active) enzymes, respectively. With the finding that these domains catalyzed a copper-dependent oxidative reaction[4,16], the name polysaccharide monooxygenase, or PMO, was adopted, and the GH61 and CBM33 enzymes were reclassified in the Carbohydrate-Active enZyme (CAZy) database as Auxiliary Activity families 9 and 10 (AA9 and AA10), respectively[17]. Some investigators then began using the names lytic PMO or LPMO. It was discovered that many AA10 enzymes could oxidize cellulose, either exclusively or in addition to chitin[10,18]. Fungal PMOs active on chitin[12] and starch[19] were reported and classified respectively as AA11 and AA13. Activity towards hemicelluloses was found in an AA9 PMO from *Neurospora crassa*[20]; this is not strictly a new activity as oxygen insertion still occurs at a β-1,4-glycosidic bond, as in cellulose. This was also the only PMO known to cleave soluble cellooligosaccharides until the recent characterization of an ortholog[21].

Recent studies have emerged linking AA10 PMOs to bacterial pathogenesis. Two enzymes, GbpA and lmo2467, had previously been described as virulence factors for *Vibrio cholerae* and *Listeria monocytogenes*, respectively[22,23] and have now been characterized as chitin-active PMOs[24,25]. Putative PMOs have also been implicated in virulence associated with *Pseudomonas aeruginosa*, *Serratia marcescens*, and *Enterococcus faecelis*[26]. A predicted PMO was recently implicated in viral pathogenesis: Chiu *et al.* reported the structure of fusolin[15], a viral spindle protein found in insect poxviruses that had been classified as AA10 in CAZy along with gp37 from baculoviruses. Both gp37 and fusolin have been previously found to bind to purified chitin[27,28].

Fusolin PMO activity has yet to be demonstrated; however, recombinantly expressed fusolin enhances infectivity of insect viruses, while variant fusolin constructs with disrupted metal-binding sites do not enhance virulence[27].

Phylogenetic analyses have yet to elucidate many of the evolutionary relationships among PMO families (Figure 1.1); such studies are challenging due to low amino-acid homology[29]. Book *et al.* have proposed that AA9 and AA10 families share an ancient ancestral protein and that current selection pressures are driving the expansion of cellulolytic capabilities in AA10 proteins[30]. Intense competition between fungi and bacteria for the same ecological niches could have fostered the spread of PMO genes; although horizontal gene transfer in eukaryotes is not well understood, transfers between bacteria and fungi have been known to occur[31]. The discovery of PMOs in viruses suggests additional vectors for PMO gene transmission.

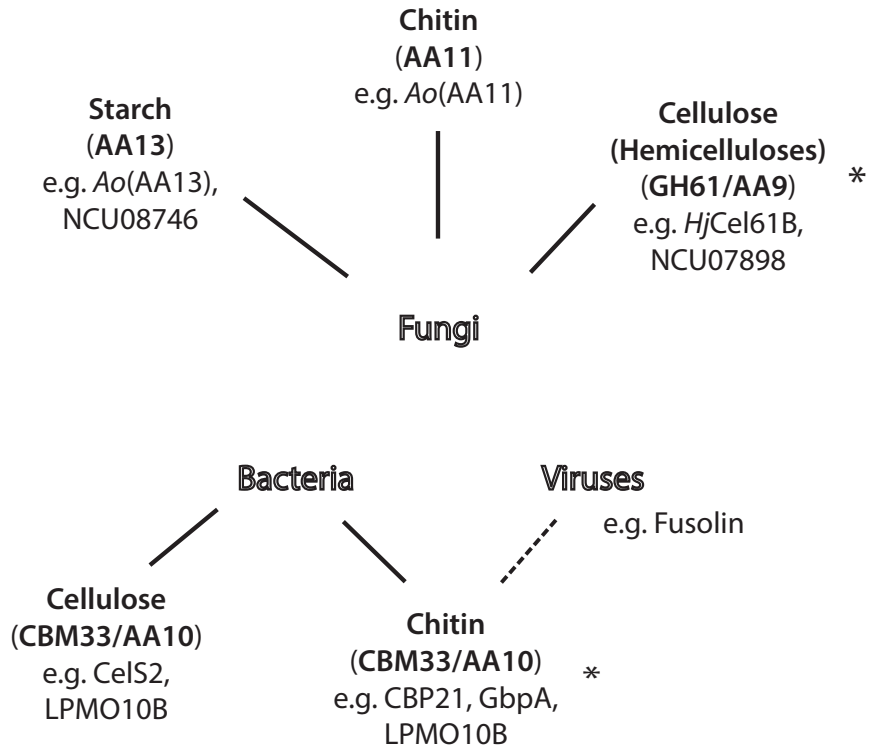

Figure 1.1. Schematic of PMO families identified to date. A subgroup of cellulose-active fungal PMOs cleaves β-1,4-glycosidic bonds in hemicelluloses. Some bacterial PMOs are active on both cellulose and chitin. Viral fusolins are classified by sequence and structure homology; chitin activity has not yet been demonstrated. Families that contain PMOs implicated in pathogenesis (in addition to those associated with biomass processing) are marked with an asterisk. Domain annotations in parentheses.

The PMO domain

The catalytic domain of PMOs resembles both fibronectin type III (FnIII) and immunoglobulin (Ig) domains (Figure 1.2). Both are β-sandwich modules of 80–100 amino acids forming seven to nine anti-parallel β -strands with Greek key motifs[32,33]. Their common jelly roll

fold is widely distributed in all life forms and regularly found in extracellular proteins[34]. Protected hydrophobic cores, inter-strand backbone hydrogen bonds, and the presence of disulfide bridges (in the case of Ig domains) contribute to structural stability. *Beta*-hairpins and longer loops conjoin adjacent strands; these are perhaps most notable as the complementarity determining regions (CDRs) in antibodies and T-cell receptors.

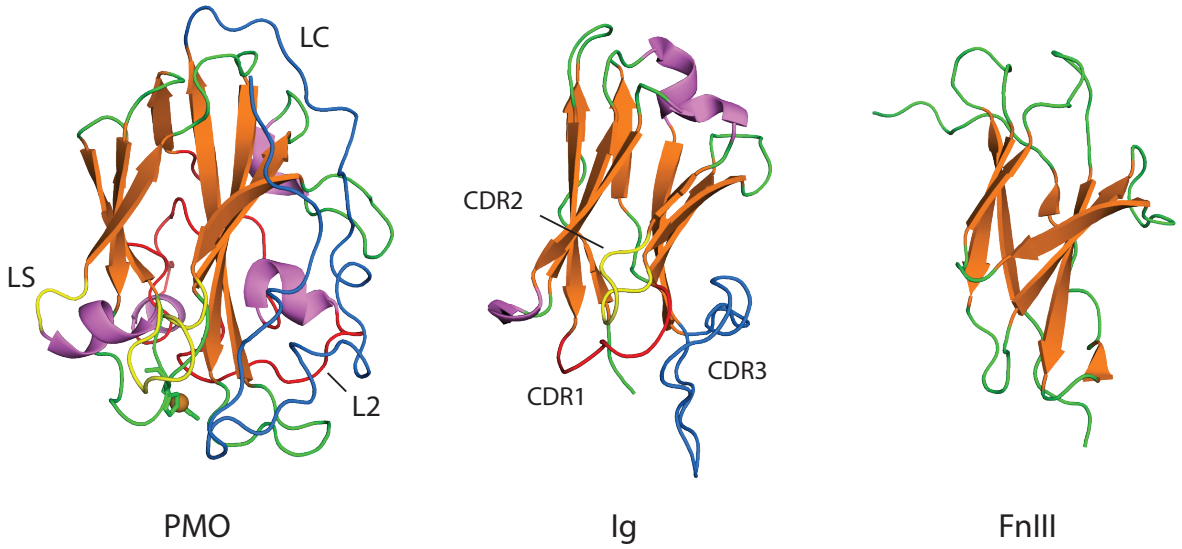

Figure 1.2. A PMO domain compared to Ig and FnIII domains. AA9 *Nc*PMO3, Ig, and FnIII (PDB IDs 4EIS, 4O5I, and 3MPC, respectively) colored by secondary structure**.** Cellulose-active fungal (AA9) PMOs contain three extended loop regions, colored red (L2), yellow (LS), and blue (LC). The Ig domain is from the variable heavy chain of a Fab; the three complementarity determining regions are also colored red (CDR1), yellow (CDR2), and blue (CDR3).

The PMO domain is a similarly stable β-sandwich of seven to nine β-strands but displays longer and more variable loop regions (Figure 1.2). PMO domains usually comprise 200–250 amino acids, but the total residue count depends on cumulative loop length. A small bacterial PMO has been reported at only ~15 kDa; homology modeling suggests abbreviated loop features limit its size[35]. Like the Ig fold, the PMO fold contains disulfide bonds, typically two or three. Scattered throughout the β-sandwich interior are conserved tyrosine and tryptophan side chains, similar to those found in the hydrophobic core of FnIII domains[33].

Most structural variation among PMOs occurs in loop regions[8]. Loop variation is particularly evident in segments that compose the substrate-binding interface (e.g. L2, LS, and LC; Figure 1.2) and is thought to be an evolutionary response to selective pressure around substrate availability[30]. While the obstacle of co-crystallization with insoluble substrates has prevented observation of their binding interactions, substrate-specific surface complementarity has been surmised from PMO structures (Figure 1.3). In the fungal enzymes, flat substrate-binding planes contain solvent-exposed aromatic (cellulose-active) and hydrophilic (chitin-active) side chains that are believed to π-stack with the glucose units of cellulose and hydrogen-bond with the acetyl moieties of chitin, respectively[3,7,12]. Crystallization of a cellulose-active PMO with cellohexaose

confirmed that a CH–π interaction with a tyrosine residue facilitates binding even with the 6-mer; additionally, a lone pair-π interaction between the substrate and His1, respectively, along with multiple other H-bonding interactions in the vicinity of the second conserved histidine in the active site (Figure 1.4) are responsible for substrate positioning[36]. The starch-active PMO contains a shallow groove at the active site that could accommodate various helical structures that starch substrates form[13,19]. Bacterial cellulose-active PMOs retain the hydrogen-bonding residues of the chitin-active AA10 enzymes but appear to be accumulating surface substitutions for cellulose binding[10,30]. AA10 enzymes also contain an α-helical protuberance in the loop between the first and second β-strands (L2) that is more exaggerated in cellulose-active enzymes[10].

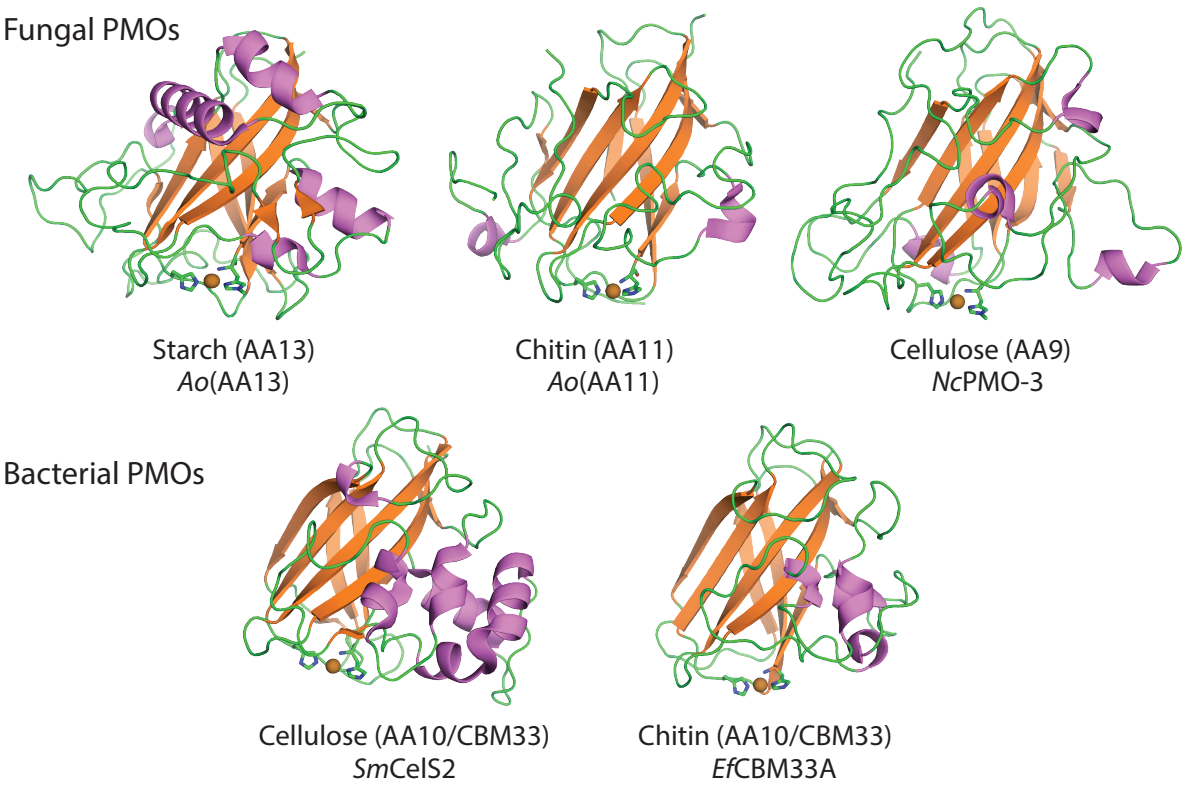

Figure 1.3. PMO domains representative of each family. Colored by secondary structure, AA13 (PDB ID 4OPB), AA11 (PDB ID 4MAI), AA9 (PDB ID 4EIS), cellulose-active AA10 (PDB ID 4OY7), and chitin-active AA10 (PDB ID 4ALC).

Differences in loop substructures in the substrate-binding plane may be responsible for regioselectivity differences in AA9 PMOs; the loop L2 (here between the second and third β-strands) is necessary for C4 oxidation in one enzyme from *Neurospora crassa*[7,37]. Factors in addition to substrate positioning may contribute to regioselectivity. The axial tyrosine, which is part of the second putative ET pathway of C4-oxidizing AA9 enzymes, has been proposed to stabilize more highly-oxidizing intermediates that might be required for hydrogen-atom abstraction from C4, which has a higher (~8 kcal/mol) estimated C-H bond enthalpy than C1[29,38,39].

Glycosylation and C-terminal carbohydrate binding modules (CBMs) also probably help recruit substrates to the active site[40]. PMOs contain other C-terminal domains, some of unknown function. The FnIII-like domains found tethered to bacterial PMOs are structurally similar to CBMs, but lack surface-exposed aromatic residues that facilitate carbohydrate-binding[33]. FnIII modules of GbpA in *V. cholerae* have been shown to facilitate attachment to the host intestinal epithelium[41]. The fusolin structure suggests its novel C-terminal region functions in maintaining viral spindle assembly and regulating PMO activity[15].

Altogether, the architecture of the PMO domain is a fitting framework for PMO catalysis: the core, engineered for stability in extracellular environments, and the loops, with their substrate-complementary motifs, provide infrastructure for a highly reactive copper center, making it a robust and specific catalyst.

PMO active sites

The PMO active site has been described in detail[29,38]. It contains a mononuclear type II copper center coordinated by three equatorial nitrogen ligands in a histidine brace motif similar to the high-pH form of the Cu(II) site in the bacterial homeostasis protein CopC[42]. The histidine brace is absolutely conserved and has come to be a defining characteristic of a PMO. The N-terminal histidine is N_{ε}-methylated in fungal PMOs, while bacterial PMOs do not appear to have this modification. Fungal PMOs expressed in hosts that do not perform the methylation are still active. Functions attributed to N_{ε}-methylation have been described elsewhere[29,43].

The PMO reaction involves two separate, one-electron reductions; in fungi, electron transfer to PMOs can occur via a large, multi-domain heme protein, cellobiose dehydrogenase (CDH)[16] . During a catalytic cycle, the Cu(II) center must undergo reduction to Cu(I) prior to activating O_2; the enzyme then, in some order, performs hydrogen-atom abstraction (HAA) and oxygen insertion on the substrate C-H bond, as well as reduces the second oxygen atom to H_2O.

Photoreduction of the copper to Cu(I) has been a common phenomenon in X-ray crystal structures, and so other spectroscopic techniques such as X-ray absorption spectroscopy (XAS) have been helpful in determining PMO coordination geometries[9,44]. Oxidized PMOs contain additional ligands coordinating the Cu(II) in a distorted octahedral or trigonal bipyramidal geometry. These can include the oxygen atom of the axial tyrosine and up to two additional oxygen ligands from the solvent. Reduced PMOs have decreased coordination numbers consistent with Cu(I) coordination preferences and predominantly are three-coordinate, T-shaped in the histidine brace.

All PMO families observed to-date have conserved active-site hydrogen-bonding (H-bonding) residues that interact with active-site water molecules and the active-site tyrosine ligand (when present) (Figure 1.4). Suggested functions of these residues include stabilization of the second histidine ligand, H-bonding to a substrate bound in the available equatorial position, and alteration of the electronic environment of the copper center[38]. A relationship between different H-bonding networks and regioselectivity has been proposed for cellulose-active bacterial PMOs[10]. Other possible functions include facilitating oxygen activation and proton-coupled ET during catalysis. If analogous to those found in cytochrome P450s, H-bonding networks in PMOs could govern the type of reactive oxygen intermediate generated in the catalytic cycle[45].

Two AA9-type PMO structures have included models of dioxygen species in the active site[7]. PMOs photoreduced by the X-ray beam during data collection may activate the dissolved O_2 in

aerobically grown crystals. The distances (>2.9 Å) observed between these species and the copper centers preclude formal bonding, however, and it is unclear whether their position near the solvent-accessible axial site is indicative of the true intermediate geometry or is an experimental artifact (Figure 1.4).

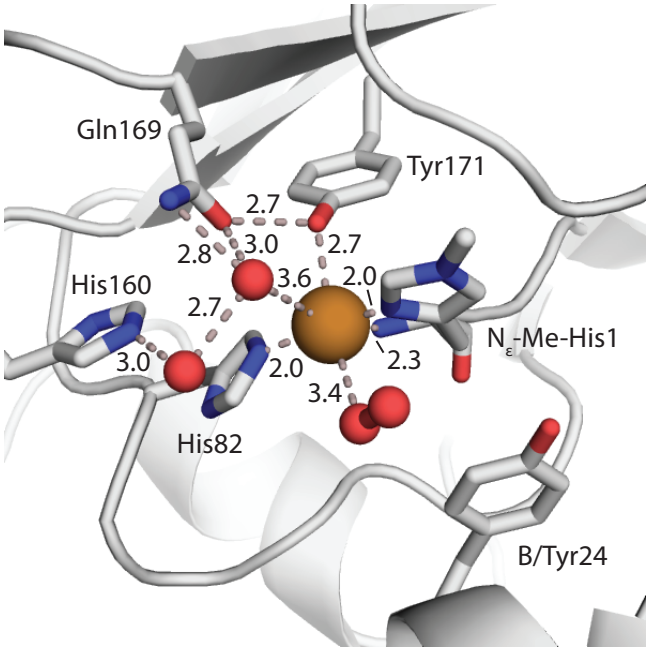

PMO family	H-bonding motif
Fungal, cellulose (AA9)	H-X_8-Q-X-Y
Bacterial, chitin (AA10)	E ... N-X-F
Viral, predicted chitin (AA10)	R-X_5-E-X-F
Bacterial, C1 cellulose (AA10)	R-X_4-E-X-F
Bacterial, C1/C4 cellulose (AA10)	H-X_2-Q-X-Y
Fungal, chitin (AA11)	N-X-E-X-Y
Fungal, starch (AA13)	Q-X_2-Q-X-Y

Figure 1.4. Active site of AA9 PMO and secondary sphere hydrogen-bonding motifs by family. The Cu(II)-like elongated octahedral coordination in *Nc*PMO3 comprises axial tyrosine and peroxide ligands and an equatorial water ligand (all of which are observed at distances that preclude formal bonding, indicative of partial photoreduction by the X-ray beam). The conserved active-site hydrogen-bonding (H-bonding) network involves H160, Q169, and Y171, in a H-X_8-Q-X-Y motif, as well as two crystallographic water molecules. In bacterial, chitin-active PMOs the conserved glutamine is ~130 residues prior to the N-X-F motif and H-bonds with the conserved asparagine on one side and the equatorial water on the other. AA9 is *Nc*PMO3 (PDB ID 4EIS). Distances are in angstroms (Å).

Thesis Research

Lignocellulose is an abundant renewable resource that could serve as a feedstock for microbially derived fuels, chemicals, and materials. The technological obstacle to its use is broadly considered to be in the conversion of plant polysaccharides to fermentable sugars. Ascomycetous filamentous fungi are prodigious degraders of cellulose; of these organisms, *Neurospora crassa* has served as both as a model system for cellulose degradation studies and a model genetic organism. Functional genomics work targeting the cellulolytic system in *N. crassa* enabled the discovery of PMOs by two former graduate students in the Marletta lab, Will Beeson and Chris Phillips. Much of the work that follows here would have not been possible without the exceptional

discoveries made by these two, with expert faculty guidance in enzyme mechanism and fungal biology from Michael Marletta and Louise Glass, respectively.

After the initial discovery and characterization of cellulose-active fungal (AA9) PMOs, the two areas that stood out as needing further investigation are 1) the PMO mechanism and 2) further PMO discovery. The PMO reaction mechanism is currently a matter of debate, but all plausible pathways require the delivery of electrons, protons, dioxygen, and the polysaccharide substrate to the active site. Taking a structural perspective, I hypothesized that conserved residues near the active site are poised to facilitate the delivery of reactants or redox equivalents to the copper center, and alteration of these side chain functionalities should impair one or more reaction steps, shedding light on the overall mechanism. The ensuing study, reported in Chapter 2, probed variants of the secondary coordination sphere via a variety of biochemical and biophysical methods and characterized their role in O_2 activation.

As described above, the active-site bonding network in the secondary coordination sphere is a conserved feature of not just AA9 PMOs, but the entire PMO superfamily. In *N. crassa* alone, PMOs active on cellulose, hemicelluloses, chitin, and starch have been characterized. The use of PMOs as catalysts for bond cleavage in a variety of substrates, in addition to the growing body of research suggesting that PMOs function in a wide range of physiological processes, begs the question of what other PMOs might exist. As there remain predicted PMOs even in *N. crassa* that do not cluster phylogenetically with the characterized families, I focused my efforts here. In Chapter 3, I begin to describe a new family of PMOs that I hypothesize plays an essential role in cell wall remodeling during hyphal fusion.

PREVIOUSLY PUBLISHED MATERIAL

This chapter was modified from a previously published review co-authored by Michael A. Marletta. Thanks to the co-author and publishers at Current Opinions in Structural Biology for allowing use of this material[46].

CHAPTER TWO: THE ROLE OF THE SECONDARY COORDINATION SPHERE IN A FUNGAL PMO

ABSTRACT

Polysaccharide monooxygenases (PMOs) are secreted metalloenzymes that catalyze the oxidative degradation of polysaccharides in a copper-, oxygen-, and reductant-dependent manner. Cellulose-active fungal PMOs degrade cellulosic substrates to be utilized as a carbon source for fungal growth. To gain insight into the PMO mechanism, the role of conserved residues in the copper coordination sphere was investigated. Here we report active-site hydrogen-bonding motifs in the secondary copper coordination sphere of *Mt*PMO3*, a C1-oxidizing PMO from the ascomycete fungus *Myceliophthora thermophila*. A series of point substitutions that disrupt this conserved network are used to interrogate its function. Activity assays, in conjunction with EPR spectroscopy, demonstrate that residues H161 and Q167 are involved in stabilizing bound oxygen, and H161 appears to play a role in proton transfer. Additionally, Q167 increases the ligand donor strength of Y169 to the copper via a hydrogen-bonding interaction. Altogether, H161 and Q167 are important for oxygen activation, and the results are suggestive of a copper–oxyl active intermediate.

INTRODUCTION

Cellulose degradation in fungi is accomplished by an ensemble of cellulose-active enzymes that are secreted to the extracellular space following induction by cellulosic metabolites[47,48]. These enzymes largely consist of hydrolytic exo- and endoglucanases working in concert with the recently discovered class of redox enzymes called polysaccharide monooxygenases (PMOs, also referred to as lytic polysaccharide monooxygenases, or LPMOs)[49]. Fungal PMOs that are active on cellulose (also known as AA9 enzymes) utilize a flat protein surface centered around the catalytic site to bind to the surface of crystalline cellulose. PMOs are the only enzymes known to degrade bulk cellulose without the need to separate one glucan from the matrix, a task that is thermodynamically difficult due to the dense network of hydrogen bonds (H-bonds) and van der Waals forces that pack glucans into microfibrils and higher-order structures[3,50]. PMOs act synergistically with hydrolytic cellulases, and thus have commercial value in enhancing cellulose degradation for the production of renewable fuels and chemicals[3]. Moreover, PMOs represent a newly discovered enzyme superfamily with novel catalytic features that are yet to be fully understood[46].

$$R{-}H + O_2 + 2e^- + 2H^+ \xrightarrow{\text{PMO-Cu}} R{-}OH + H_2O$$

Figure 2.1. The polysaccharide monooxygenase (PMO) reaction. R–H = substrate (*e.g.* cellulose).

PMO activity is copper-, oxygen-, and reductant-dependent, and reaction products show incorporation of one oxygen atom from O_2, consistent with monooxygenase activity[16,51] (Figure 2.1). Although the PMO chemical mechanism is unknown, it has been postulated to be similar to other monooxygenases such as peptidylglycine α-hydroxylating monooxygenase or cytochrome P450 enzymes[29]. The generally agreed-upon mechanisms for these enzymes differ in their reactive intermediates and catalytic steps, but all require the well-timed delivery of oxygen (O_2), electrons,

and protons to the active site[52–54]. Active-site structures of O_2-activating copper (Cu) enzymes are known to tune reactivity in various ways[55], and the distinctive features of the PMO active site may be integral to the reaction mechanism. PMOs possess a type II Cu center, coordinated by a histidine brace motif, in which two absolutely conserved histidine side chains (one being H1, which possesses a unique N_ε-methylation) and the *N*-terminal amino group ligate the Cu. In the AA9 family, a conserved tyrosine also occupies the primary coordination sphere, axial to the histidine coordination plane. The secondary coordination sphere comprises a conserved hydrogen-bonding (H-bonding) network, as deduced from AA9 crystal structures[4,7,8].

Non-covalent secondary sphere effects on catalysis in metalloenzymes can arise from steric, electrostatic, and H-bonding interactions; among these, H-bonding is thought to be the most important[56,57]. Hydrogen bonds formed by secondary sphere residues in O_2-binding proteins are known to stabilize bound O_2, as in the classical case of the distal histidine in hemoglobin and myoglobin[58]. In O_2-activating enzymes, H-bonds in the secondary coordination sphere help tune redox potentials and ligand donor strengths, facilitate proton and electron transfer, and help stabilize nonstandard coordination geometries and high-energy intermediates[56]. In cytochrome $P450_{cam}$, for example, H-bonding residues in the proximal pocket tune the redox potential of the heme[59], and those in the distal pocket control proton transfer to reactive iron-bound oxygen-based intermediates[45].

PMO crystal structures have revealed that secondary sphere residues form conserved active-site H-bonding networks with buffer and solvent molecules[4,7,8,14]. One early study found that a PMO with a second-sphere glutamine-to-leucine substitution failed to stimulate cellulase activity compared with the wild type protein[3]. However, the conclusions of this study are somewhat incomplete as neither Cu nor reductant was present in the assay, except possibly as a contaminant. Herein, we investigate the role of the secondary coordination sphere in PMO mechanism via structural, bioinformatic, biochemical, and spectroscopic methods. We term the PMO used for these studies *Mt*PMO3*, as it is a member of the C1-oxidizing PMO3* subtype[37] cloned from the filamentous ascomycete *Myceliophthora thermophila*. The crystal structure of *Mt*PMO3* highlights H-bonding patterns in the secondary sphere. Conserved H-bonding motifs are identified, and a panel of site-specific variants is constructed. Wild type *Mt*PMO3* and H-bonding variants are assayed for cellulose activity and O_2 consumption. Additionally, the Electron Paramagnetic Resonance (EPR) spectra of the wild type and variant proteins are utilized for mechanistic insight.

MATERIALS AND METHODS

Strains and Materials. Wild type *Neurospora crassa* (FGSC 2489) and *Myceliophthora thermophila* (ATCC 42464) were used in the experiments herein; genomic DNA from *M. thermophila* was purified using methods described by the Fungal Genetics Stock Center[60]. PASC was prepared as previously described[16].

Protein Expression and Purification. *Mt*PMO3* constructs were expressed in *Neurospora crassa* using a knock-in expression method, as previously described[61]. Point substitutions were introduced using site-directed mutagenesis to a pCSR-1 vector containing wild type *Mt*PMO3* (gene ID MYCTH_92668, isolated from *M. thermophila* genomic DNA). Mutagenesis products were transformed into *E. coli* DH5α cells for propagation, and sequence-validated linearized target DNA constructs were transformed into *N. crassa* for expression. Protein constructs were purified from

the *N. crassa* secretome as described for wild type *Mt*PMO3*[37]. Before the final gel filtration step, enzymes were reconstituted with excess $CuSO_4$ at pH 5.0 for 4 hours at ambient temperature. The final chromatography step also functioned to desalt the sample of excess $CuSO_4$.

*Mt*CDH-2 was purified natively from *M. thermophila* as described previously[16].

Protein Crystallization. Wild type *Mt*PMO3* was crystallized using sitting-drop vapor diffusion techniques as implemented by an Oryx8 crystallization robot (Douglas Instruments). Crystals used for structure determination grew in the presence of a crystallization cocktail consisting of 18% PEG 6000 (w/v) and 0.1 M citric acid, pH 3.9 at 4 ˚C. 150 nL of crystallization cocktail was mixed 1:1 with 20 mg/mL of *Mt*PMO3*. Prior to flash-freezing in liquid nitrogen, crystals were soaked briefly in 25% PEG 6000 (v/v in water) as a cryoprotectant.

Data Collection and Structure Determination. X-ray diffraction data was collected at beamline 12-2 at the Stanford Synchrotron Radiation Lightsource (SSRL). Data were processed with Denzo/Scalepack programs from the HKL 2000 software package[62]. Initial phases were obtained by molecular replacement with a search model based on the structure of Cel61B (PDB ID 2VTC), a PMO from the soft-rot fungus *Hypocrea jecorina*[4]. The model for *Mt*PMO3* was built using COOT[63] and refined using Refmac5 within the CCP4 package[64]. The statistics of the diffraction data and structure refinement are summarized in Table 2.1.

Identification of conserved H-bonding networks. Multiple sequence alignment (MSA) datasets for each PMO family were generated using a Hidden Markov Model-based search algorithm[65]. Search ensembles consisted of smaller, starting MSAs containing protein sequences of structurally or functionally characterized PMOs. Conserved residues were examined against existing structures of each PMO family to identify conserved sequence motifs near the active site engaging in conserved H-bonding interactions.

Cellulose Activity Assays. Wild type and variant *Mt*PMO3* (2 µM) was mixed with 10 mg/mL phosphoric acid swollen cellulose (PASC) and 1 µM *Mt*CDH-2 with atmospheric O_2. Reactions of 45 µL were carried out in 50 mM sodium acetate buffer (5.0) at 40 ˚C for 1–30 minutes. Peaks from aldonic acids with degrees of polymerization of (DP) 5–13 were analyzed via HPAEC-PAD as described previously[16]. Products were quantified by integrating peak areas with Dionex Chromeleon software v. 7.1.3. Smaller C1-oxidized products with DP 2–4 were excluded from analysis, as they are also products of the CDH reaction.

O_2 Consumption Assays. An Oxygraph Plus System (Hansatech Instruments) equipped with a water jacket was used to measure O_2 levels in *Mt*PMO3* reactions over time. Assays containing 0.5 µM *Mt*PMO3*, 10 mg/mL PASC, and atmospheric O_2 were conducted in 50 mM sodium acetate buffer (5.0) at 40 ˚C. Reactions of 300 µL were initiated with 5 µM *Mt*CDH-2. Stir bar speed was set to 70 rpm. O_2View software was used for data analysis. Initial rates were calculated using 20 s intervals within the first two minutes of the reaction.

Peroxide Formation Assays. Horseradish peroxidase (HRP)-coupled assays were based on previously described methods[66], utilizing Amplex Red as a substrate for the photometric detection of peroxide in *Mt*PMO3* reactions over time. Assays contained 100 µL of 100 mM HEPES (7.0), 0.5 µM *Mt*PMO3*, 0.5 U/mL HRP, 50 µM Amplex Red, 0.5 µM MtCDH-2, 100 µM cellobiose, and ± 25 U/mL superoxide dismutase (SOD). Reactions were carried out in flat-bottom, untreated 96-well plates (Corning), and detection at 573 nm was performed with a SpectraMax 340 plate reader (Molecular Devices) and analyzed with SoftMax Pro software.

Electron Paramagnetic Resonance Spectroscopy. All variant and wild type *Mt*PMO3* samples (200–300 μM) were prepared in 10 mM Tris (8.5) and 150 mM NaCl with 20% glycerol. X-band continuous-wave (CW) EPR spectra were recorded on a Bruker ELEXSYS E500 spectrometer equipped with a cylindrical TE011-mode resonator (SHQE-W), an ESR-900 liquid helium cryostat, and an ITC-5 temperature controller (Oxford Instruments). Spectral simulations were performed with MATLAB Release 2016A using the EasySpin 5.1.5 toolbox.

Accession Numbers. Coordinates and structure factors have been deposited in the PDB with accession number 5UFV.

RESULTS AND DISCUSSION

Structure of *Mt*PMO3*. The X-ray crystal structure of *Mt*PMO3* was determined to 2.45 Å resolution and contained six non-crystallographic symmetry-related molecules in the asymmetric unit (*i.e.* chains A–F). Like other PMO structures, it exhibits an overall β-sandwich fold consisting of two β-sheets formed by an anti-parallel arrangement of nine β-strands (Figure 2.2a). These are interspersed with extensive loop regions, many of which exhibit high crystallographic B-factors (~50 $Å^2$), indicating disorder. Two disulfide bonds (Cys48–Cys172 and Cys 87–Cys94) anchor smaller loop features to the β-sandwich.

The Cu active site of *Mt*PMO3* is located in the center of a flat substrate-binding surface (~500 $Å^2$) and shares the primary coordination sphere features of other fungal PMOs, including the histidine brace (H1 and H75), axial tyrosine residue (Y169), and *N*-terminal histidine methylation. The tyrosyl O atom is positioned 2.7 Å from the Cu ion, which falls within the range of Y169(O)---Cu distances observed in crystal structures of other AA9 enzymes. These distances are too long to be formal bonds even with a Jahn-Teller distortion[67], and it is unclear whether this elongation is a feature of the Cu(II) coordination sphere or represents a loss of the Y169(O) ligand due to photoreduction. Additional solvent-derived ligands are not observed in the active site shown in Figure 2.2 (*Mt*PMO3* chain C), which may result from a lack of strongly identifiable water content at the structure resolution, or again from Cu being in the reduced state. Deviations from expected disulfide bond lengths and Cu(II) coordination geometries strongly imply that X-ray induced photoreduction occurred during data collection. The estimated diffraction-weighted X-ray dose was ~10 MGy[68], which exceeds the doses (~1 MGy) observed to reduce Cu centers in bacterial PMOs[11].

The polypeptide chains (A–F) exhibit overall good agreement with each other and result in a pairwise C_α RMSDs <0.2 Å over all 228 residues. The amino acids of each chain are numbered according to the sequence of the mature polypeptide (translated from gene ID MYCTH_92668), beginning with the *N*-terminal histidine residue (*i.e.* H1). The most *C*-terminal ten residues of each chain were not modeled due to a lack of observable electron density.

The LS loop of chain D was best modeled in a slightly different conformation than that of the other five chains; it also exhibits poor electron density for some residues and contains outliers for both Real-space R-value Z-scores (RSRZ) (T115) and Ramachandran analyses (D112). These discrepancies are due to a crystal packing artifact in which the carboxylate moiety of D112 extends to form a H-bond with D13 and T69 residues on chain F, thereby distorting the rest of the LS loop of chain D. The final structure contains additional Ramachandran outlier prolines or proline adjacent residues (P33, D34, P170) that appear necessary to accommodate the unique stereochemical constraints of these proline side chains.

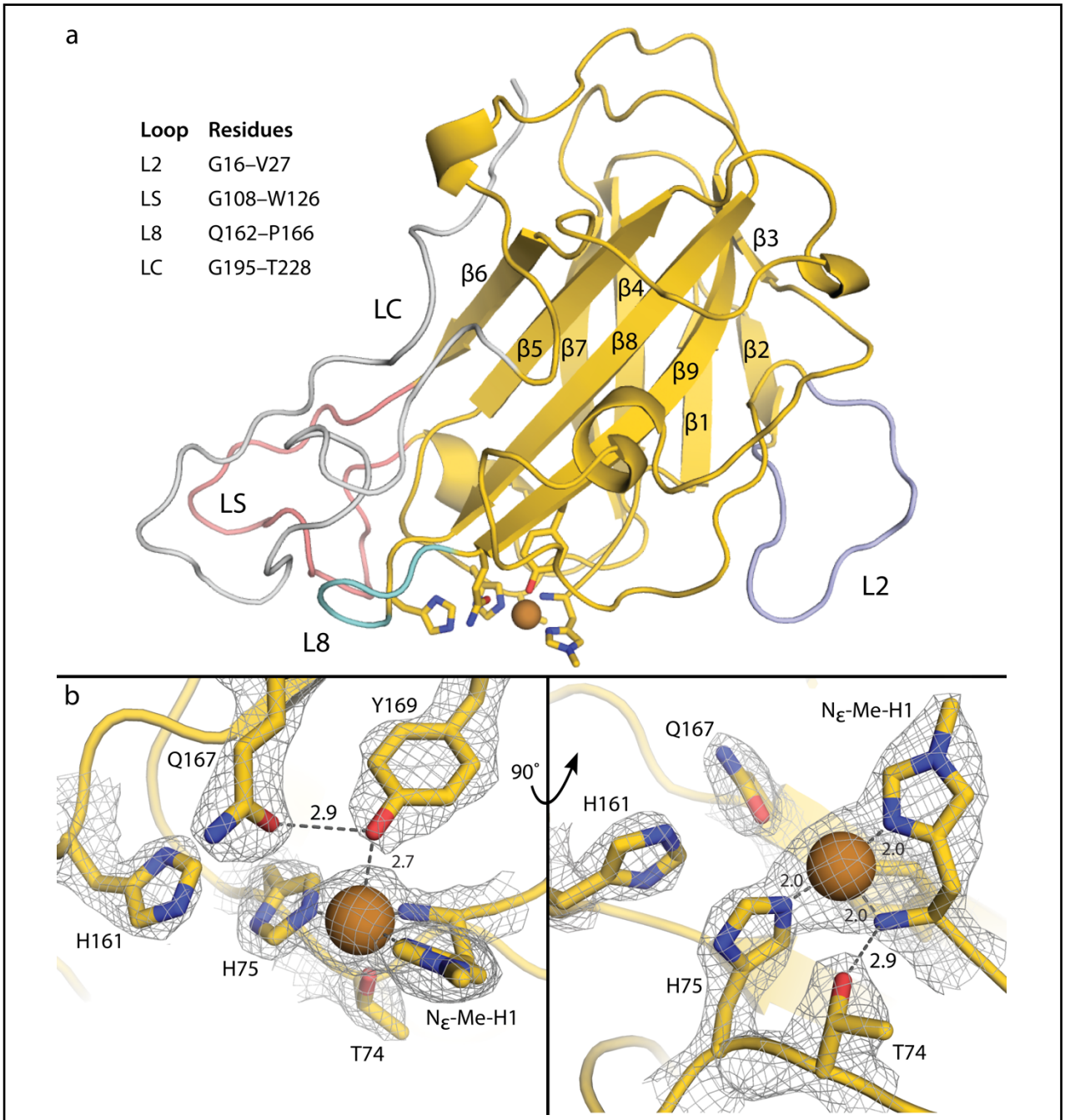

Figure 2.2. Crystal structure of *Mt*PMO3*. (**a**) Full structure in cartoon representation with primary and secondary coordination sphere residues as sticks. All β-strands are numbered in order of primary sequence. Relevant loop features are highlighted in lavender (L2), pink (LS), teal (L8), and silver (LC). All other carbon atoms are shown in yellow, nitrogen atoms in blue, and oxygen atoms in red. Copper ion depicted as a brown sphere. (**b**) *Mt*PMO3* active site showing primary (N_ε-Me-H1, H75, Y169) and secondary (T74, H161, Q167) sphere residues with mesh electron density map contoured to 1.5 σ. H161 and Q167 are positioned to H-bond with ligands in the solvent-facing equatorial position. Q167 H-bonds with the axial tyrosine ligand. T74 H-bonds with the *N*-terminal amino group of H1 and forms a bond with an axial solvent ligand when present. Hydrogen-bonding distances are shown in Ångstroms (Å).

Compared to other structures of fungal, cellulose-active PMOs, the structure of *Mt*PMO3* does not display any significant structural differences in the polypeptide main chain. The largest structural deviations occur in the LS and L2 loops; the latter is believed to vary according to reaction regioselectivity in the AA9 enzymes. In PMO3 enzymes that form both C1 and C4 oxidation products, the L2 loop is large and contains an α-helical segment of 5–11 residues; in *Mt*PMO3* the L2 loop is abbreviated by 5–8 residues and lacks the α-helix (Figure 2.3). This result is consistent with a previous experiment in which the L2 loop of a PMO3 was deleted, resulting in a loss of C4-oxidized products, but retention of C1 activity[37].

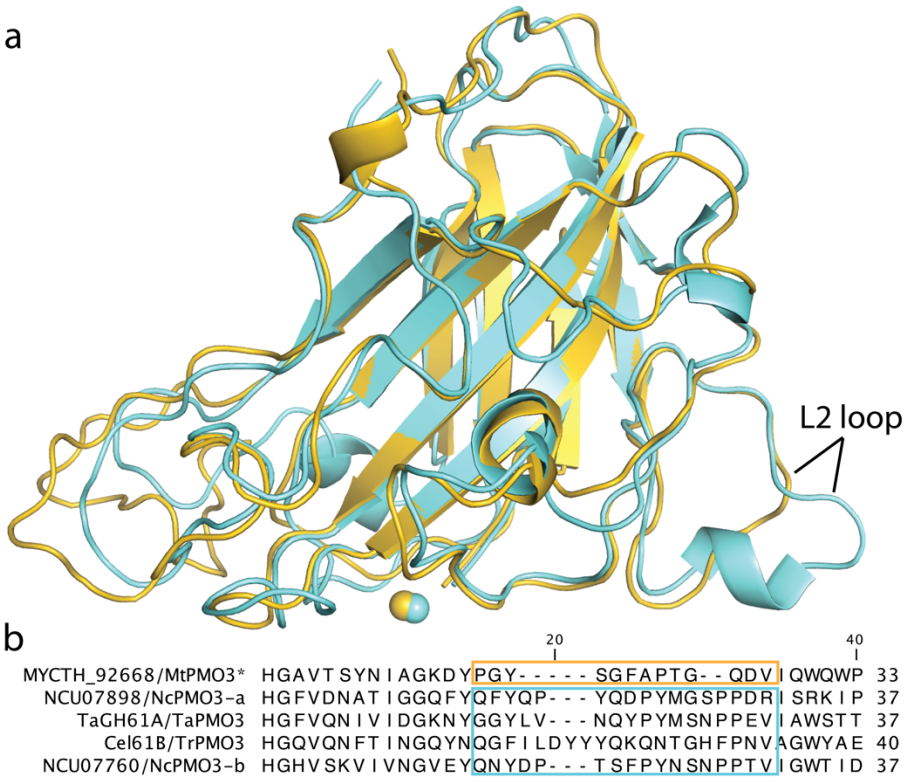

Figure 2.3. Comparison of PMO3 and PMO3*. (**a**) *Mt*PMO3* structure (yellow) superposed with *Nc*PMO3 (cyan, PDB ID 4EIS). Overall C_α RMSD ~ 0.8 Å (over 154 aligned residues). (**b**) Multiple sequence alignment of the first 40 residue positions of *Mt*PMO3* with four PMO3 sequences. The L2 loop sequences are highlighted with boxes. *Mt*PMO3* contains an abbreviated L2 loop that lacks α-helical structure compared with that of PMO3 enzymes.

One notable difference from previous PMO structures is that the side chain of H161 swings "out" rather than "in" towards the Cu in four of the six molecules in the asymmetric unit (*i.e.* chains A, B, D, and F adopt an "out" conformation). This unprecedented rotamer is stabilized by weak H-bonds with Q162 and E121 on the LS loop, which is longer in *Mt*PMO3* and extends closer to the active site when compared with other AA9 enzymes. In most chains there is weak difference electron density for the other, "inward-facing" rotamer, and the loop containing H161 (here termed L8) exhibits higher-than-average B-factors, indicating general disorder in this region. In the

remaining two molecules (chains C and E), H161 swings "in" towards the Cu and appears trapped in that conformation by a H-bonding interaction with D26 from a symmetry-related molecule within the crystal (Figure 2.4). Interestingly, a recent PMO structure also reported an aspartate from a neighboring molecule crossing over into the active site to coordinate with the Cu ion (coordination via the aspartate carboxylate O atoms which are 2.2 and 2.7 Å away)[69]. In contrast, the carboxylate moiety of D26 is 4.6 Å away from Cu in the *Mt*PMO3* structure.

The secondary coordination sphere of *Mt*PMO3* comprises residues that form a network of H-bonds around the primary coordinating ligands. These include T74, which H-bonds with the *N*-terminal amino group of H1 as well as ligands in the axial solvent-facing position; H161, which is positioned to H-bond with equatorial solvent-facing ligands; and Q167, which also H-bonds with equatorial solvent ligands and with Y169 (Figure 2.2). The H-bonding network is similar to those found in other fungal, cellulose-active PMO structures with ligands derived from the solvent or crystallization buffer (Figure 2.4a).

Identification of Conserved H-bonding Motifs in PMOs. A bioinformatics analysis combining sequence identity and structural alignment revealed conserved H-bonding networks in all fungal PMO families. All cellulose-active (AA9) enzymes contain the H-X_n-Q-X-Y motif observed in *Mt*PMO3*, whereas chitin-active (AA11) and starch-active (AA13) enzymes present N-X-E-X-Y and Q-X_2-Q-X-Y motifs, respectively (Figure 2.4b). In AA9 enzymes, the spacer region formed by loop L8, between the histidine and glutamine residues, is typically eight residues in length (n=8); however, this region is shortened to five residues (n=5) in *Mt*PMO3* and other predicted PMO3* enzymes. In crystal structures of chitin- and starch-active enzymes, the active-site H-bonding motifs share similar coordinates with the H-X_n-Q-X-Y motif in the cellulose-active enzymes with respect to the Cu center. Additionally, they retain the H-bond with the axial tyrosine residue as well as the H-bonds with ligands presented in the equatorial solvent-facing positions. Similar H-bonding networks are also present in bacterial PMOs (Figure 2.4b). Deep conservation of this H-bonding network across the PMO superfamily suggests that it performs a central role in PMO catalysis, regardless of substrate specificity. Putative mechanistic functions include stabilizing Cu-bound O_2 species or substrate, perturbing the pK_a of an intermediate species, and mediating proton transfer reactions. This network could also tune the redox properties of the Cu site.

In structures of exclusively C1-oxidizing PMOs, a threonine or tyrosine side chain accepts an H-bond from the *N*-terminal amino group; in those of C4-oxidizing PMOs, an ordered water molecule serves the same role. The T74 residue in *Mt*PMO3* forms H-bonds with the *N*-terminal amino group of H1. This interaction enhances the nucleophilicity of the *N*-terminal amino ligand and could help stabilize high-valent oxyl intermediates. Additionally, T74 may form H-bonds with ligands occupying the axial Cu coordination site *trans* to the tyrosine. In the structure of a PMO2 bound to a cellodextrin substrate, the ordered "pocket" water H-bonds with a C6-OH atom of the substrate, in addition to accepting a H-bond from the *N*-terminal amino group[36]. This "axial" H-bonding network is absent in PMO3 subtype (C1/C4-oxidizing) enzymes, where a proline residue excludes solvent from the pocket.

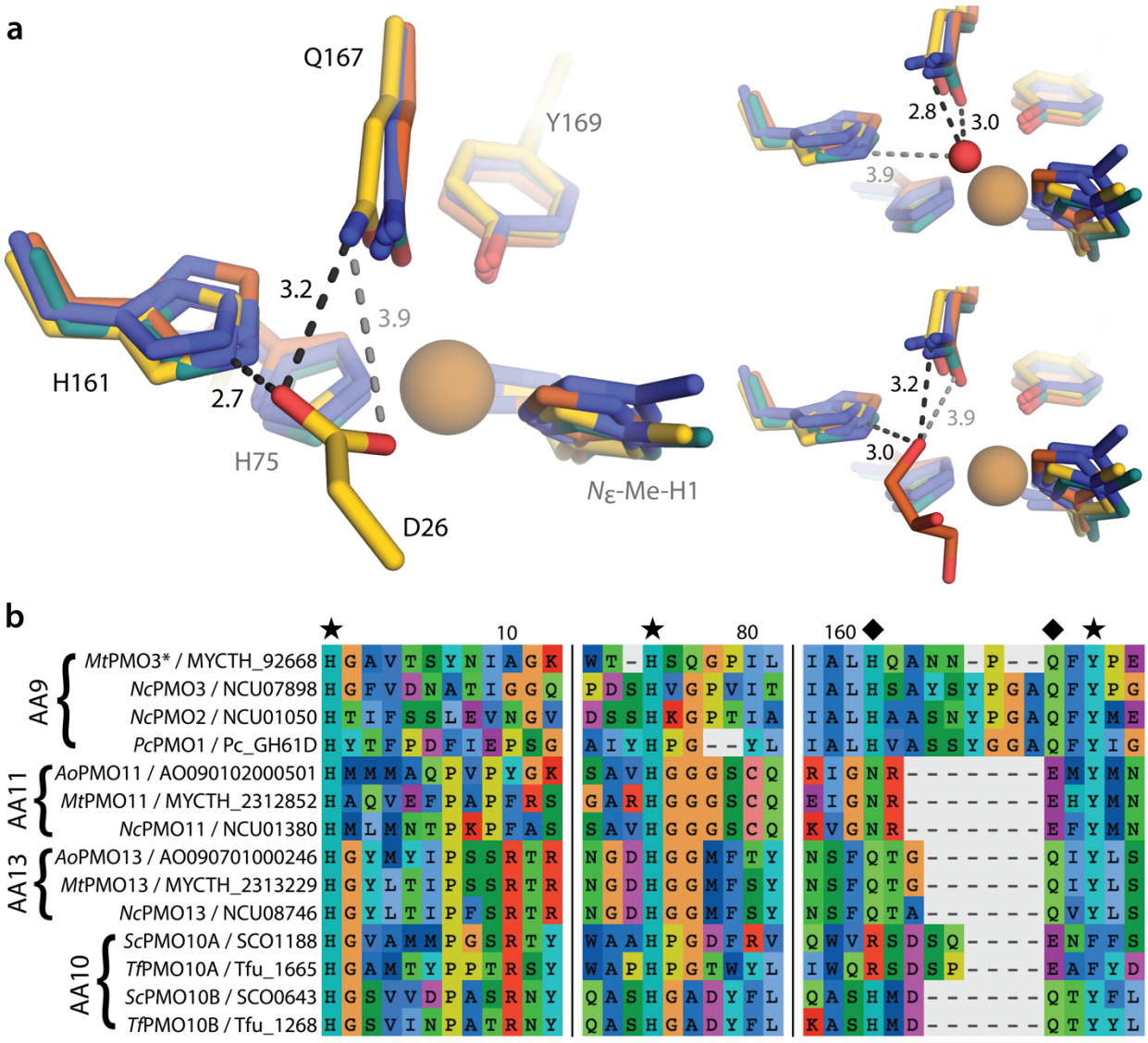

Figure 2.4. Alignments of PMO H-bonding motifs at structure and sequence levels. (a) Structural superposition of *Mt*PMO3* (yellow) with three other AA9 structures, *Pc*PMO1 (orange, PDB ID 4B5Q), *Nc*PMO2 (indigo, 4EIR), and *Nc*PMO3 (teal, 4EIS). Conserved residues H161 and Q167 (*Mt*PMO3* numbering) form H-bonds with D26 from a symmetry-related molecule in *Mt*PMO3* (left), a water molecule in *Nc*PMO3 (top right), and a buffer-derived glycerol molecule in *Pc*PMO1 (bottom right). Distances are in Ångstroms (Å). All active sites appear reduced by the X-ray beam; exogenous molecules in the equatorial position are at lengths (3.6–4.6 Å) from the Cu center that exclude formal coordination. (b) Multiple sequence alignment of representative AA9, AA10, AA11, and AA13 PMOs showing conservation of H-bonding motifs (marked with diamonds) within the PMO superfamily. Fungal PMOs possess a H-X_{5-8}-Q-X-Y (AA9), N-X-E-X-Y (AA11), or Q-X_2-Q-X-Y (AA13) motif depending on substrate specificity (cellulose, chitin, and starch, respectively). Bacterial AA10 PMOs active on cellulose contain either a R-X_4-E-X-F or H-X_2-Q-X-Y motif. Primary coordinating residues are marked with a star. Numbers correspond to *Mt*PMO3* amino acid numbering.

Cellulose Activity and O_2 Utilization of H-bonding Variants. The activity of *Mt*PMO3* variants at H161, Q167, and T74 was examined using phosphoric acid swollen cellulose (PASC) as a substrate. Assays utilized reduced *Mt*CDH-2 to deliver reducing equivalents from its flavin cofactor. Soluble products quantified at one-minute endpoints show that activity is reduced (~10–50% relative to wild type), but not abolished by any single substitution (Figure 2.5). Given the conservation of H161 and Q167, it was expected that the alanine substitutions would have a more dramatic reduction on activity. One explanation is that solvent may enter the cavity created by the difference in side chain volume and "rescue" activity to some extent via H-bonds from the solvent. This would be expected to occur in PMOs because the active site is near the protein-solvent interface. The PASC assay gives limited information because the insoluble nature of the substrate impedes quantitative kinetic analysis.

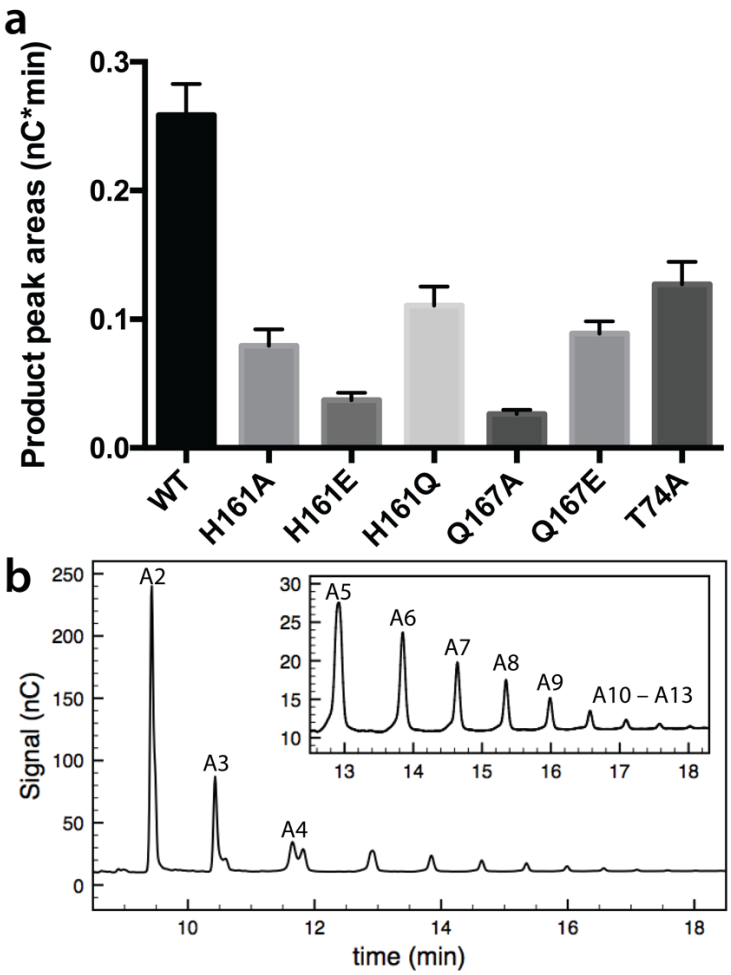

Figure 2.5. Cellulose activity assays. (a) Effect of H-bonding network substitutions on *Mt*PMO3* PASC activity. Assays contained 2 µM PMO, 10 mg/mL PASC, atmospheric O_2, and 1 µM *Mt*CDH-2 as the reducing agent. Reactions of 45 µL were carried out in 50 mM sodium acetate buffer (pH 5.0) at 40 ˚C for 1 minute. Peaks from aldonic acids with DP 5–13 were quantified via HPAEC with electrochemical detection (nC), and peak areas were integrated over time (nC•min). Smaller C1-oxidized products with DP 2–4 were excluded from this analysis, as they are also products of the CDH reaction. (n=3) (b) Sample HPAEC-PAD trace with aldonic acid products labeled by DP 2–13.

Assays were also performed with addition of exogenous Cu(II) and showed no increase in activity (Figure 2.6), demonstrating that all wild type and variant enzymes are not functionally deficient in copper, as purified.

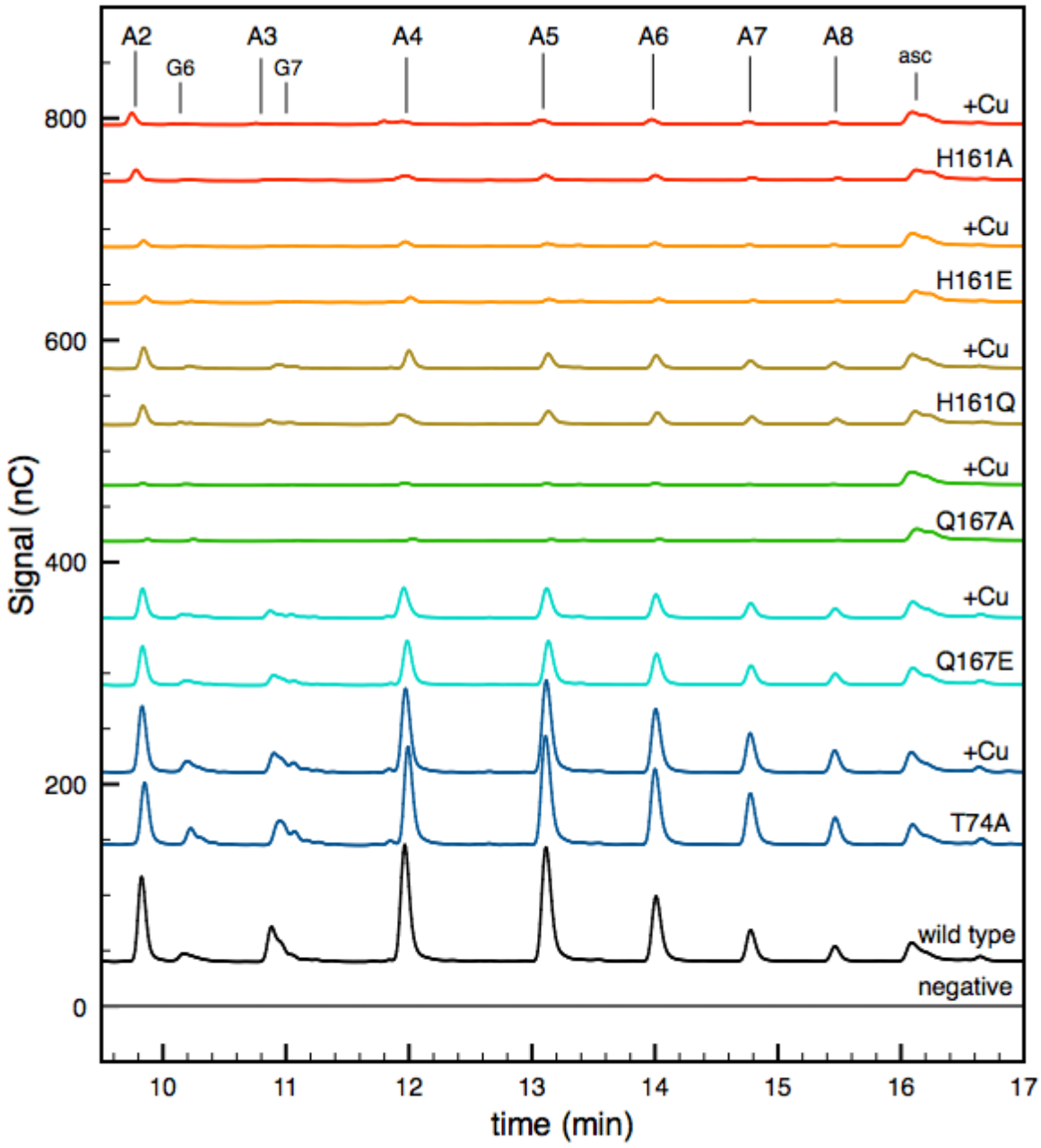

Figure 2.6. Cellulose activity assays with and without exogenous Cu(II). Assays (60 µL) contained 5 µM PMO, ± 5 µM $CuSO_4$, mg/mL PASC, atmospheric O_2, and 2 mM ascorbate as the reducing agent. Reactions were carried out in 50 mM sodium acetate buffer (pH 5.0) at 42 ˚C for 2 hours.

Initial rates of O_2 consumption were measured for all variants and ranged from ~50–100% of the wild type enzyme (Figure 2.7). Variants H161E, Q167A, Q167E, and T74A are the slowest to turn over O_2 at ~50% the rate of wild type. The other H161 variants are less affected: H161A turns over O_2 at ~70% the rate of wild type, and H161Q can turn over O_2 at rates comparable to the wild type. A number of variants show defects in O_2 consumption that are smaller than their defects in product formation. This observation is complicated by the high background in the O_2 consumption assays, as well as the difficulty in extracting rate information from the PASC assays; however, it suggests O_2 utilization is decoupled from substrate hydroxylation. The clearest example of this is the H161Q variant, followed by H161A.

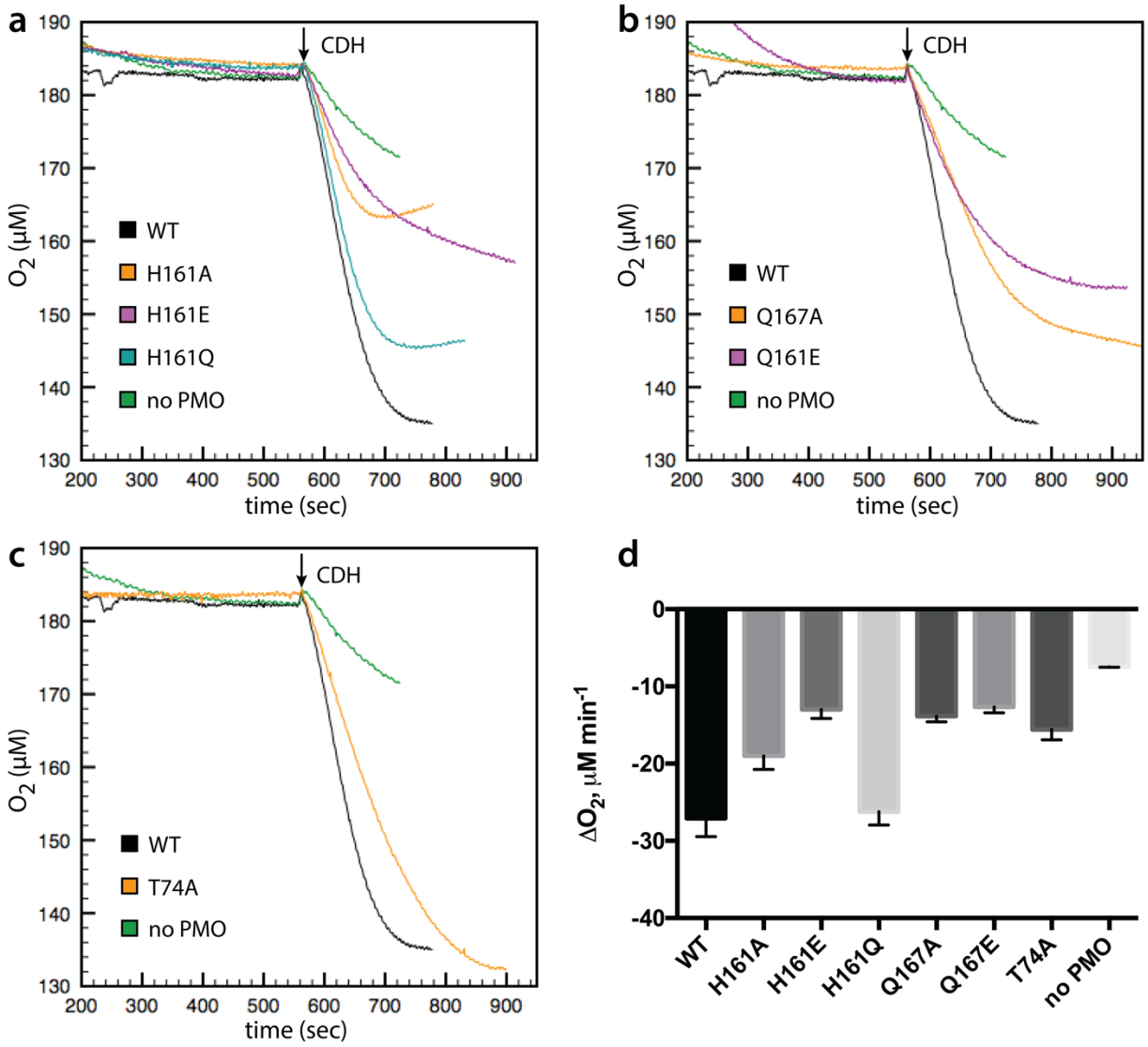

Figure 2.7. Effect of H-bonding network substitutions on O_2 consumption rate by *Mt*PMO3*. Assays contained 0.5 µM PMO, 10 mg/mL PASC, and atmospheric O_2, and were carried out in 50 mM sodium acetate buffer (pH 5.0) at 40 ˚C. Reactions of 300 µL were initiated with 5 µM *Mt*CDH-2. (**a–c**) Traces showing O_2 consumption by variants, wild type (WT), and background rate (BG, no PMO) (**d**) Rates of O_2 consumption derived from initial velocity regions. (n=3)

H161 as a H-bond donor would stabilize the Cu(II)–superoxo (Cu(II)–$O_2^{\bullet-}$) complex, the most likely species formed upon O_2 binding to reduced Cu[44], if formed at the solvent-facing equatorial coordination site. This binding site for O_2 is supported by a recent crystal structure[70]. The H161E variant introduces a carboxylate moiety that is likely to bear a negative charge at the reaction pH. Substitution of either H161 or Q167 to glutamate results in some of the lowest O_2 consumption rates, consistent with decreased O_2 turnover that would result from charge repulsion between a glutamate side chain and a negatively-charged oxygen intermediate. The H161Q substitution could retain the H-bond to stabilize O_2 binding if the rotamer overlaps with H161 placement in the wild type enzyme. Given the essentially identical rates of O_2 consumption between H161Q and the wild type, it is likely that it does overlap and that H-bond donation to the equatorial site plays a role in O_2 turnover. As significant perturbation of the amide pK_a of glutamate would be required to utilize H161Q as a general acid, it probably cannot transfer the proton, however.

It has been reported previously that PMOs produce hydrogen peroxide *in vitro* as a result of an uncoupled side reaction in the absence of substrate[66]. This result has been replicated here with both wild type and variant *Mt*PMO3* using a peroxidase-coupled assay. For the H161 variants, but not for the wild type or other H-bonding variants, addition of superoxide dismutase to the peroxidase-coupled assay results in a significant increase in peroxide formation, indicating that superoxide is present as a product of the uncoupled reaction in the H161 variants (Figure 2.8).

The combined data showing that the H161 variants exhibit decoupling and produce superoxide indicate that H161 is important for producing or stabilizing the active intermediate in *Mt*PMO3*. Beyond stabilizing the Cu(II)–$O_2^{\bullet-}$ species, it is likely that H161 plays a role in proton transfer to Cu(II)–$O_2^{\bullet-}$. Without acquiring a proton, superoxide is unlikely to be further reduced to peroxide, explaining the superoxide formation observed in all H161 variants in the uncoupled reaction. Assuming superoxide release is related to the decoupling of O_2 consumption from product formation, either Cu(II)–$O_2^{\bullet-}$ is not stable without H161, or Cu(II)–$O_2^{\bullet-}$ is not the predominant species performing hydrogen atom abstraction from the substrate. This supports a P450-like mechanism, in which the O–O bond must first be cleaved, leaving the resulting oxyl radical to abstract the substrate hydrogen atom. A Cu-oxyl species has never been directly observed in solution, but such a mechanism has been proposed for PMOs from quantum mechanical calculations[43,71]. However, the coordination geometry of the Cu–oxyl intermediate in that study, which invokes O_2 binding and cleavage at an axial coordination site, is different from that proposed here. Possible mechanisms that depend on either a superoxo or an oxyl active intermediate are depicted in Figure 2.9.

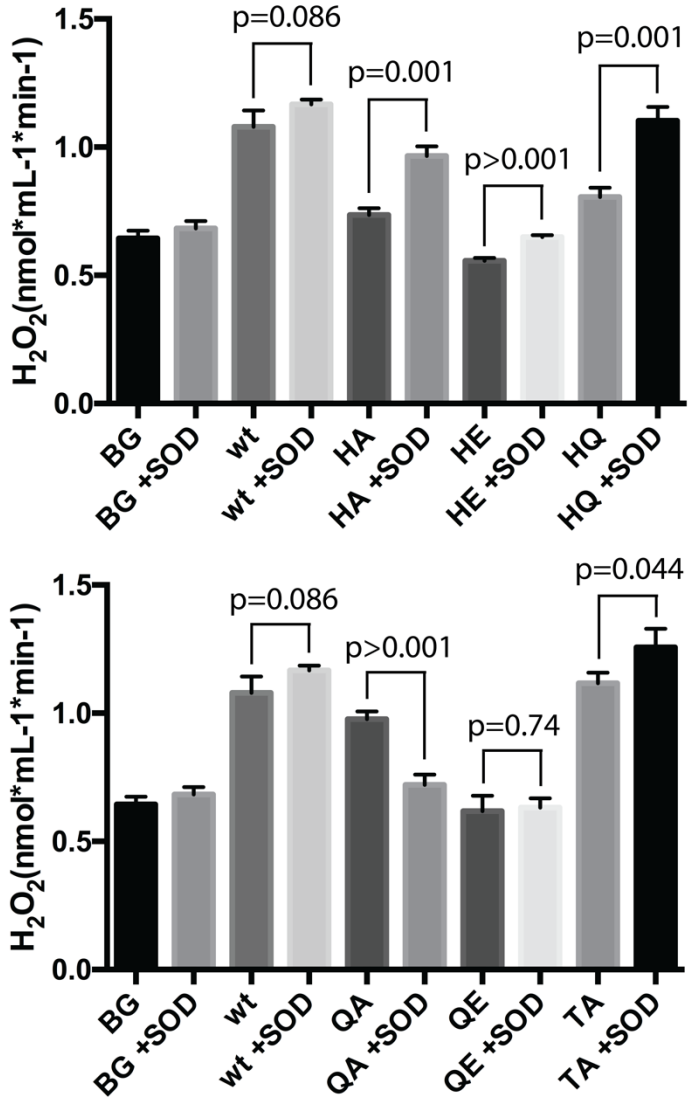

Figure 2.8 Histidine 161 variants produce superoxide. Horseradish peroxidase (HRP)-coupled assays ± superoxide dismutase (SOD) with *Mt*PMO3* variants. Assays were carried out in 100 uL of 100 mM HEPES pH 7.0 and contained 0.5 µM PMO, 0.5 U/mL HRP, 50 µM Amplex Red, 0.5 µM MtCDH-2, 100 µM cellobiose, and ± 25 U/mL SOD. BG = background, without PMO. (n=3)

The Q167 variants have the slowest rates of O_2 reduction relative to wild type, indicating that the H-bond donated to the solvent-facing equatorial site, the main feature lost in both variants, is important for O_2 turnover. Given the intrinsic pK_a of the Q167 side chain and the lack of superoxide in assays with Q167 variants, this residue is not expected to act as a general acid. Therefore, H-bond donation from the amide nitrogen probably facilitates O_2 binding. Q167A has the lowest PASC activity of all the variants reported here, but that may be partially due to electronic effects on the Cu site (*vide infra*). The reduced O_2 consumption rate of Q167E may be explained by unfavorable electrostatic interactions similar to H161E (*vide supra*) that would decrease O_2 turnover. Altogether, the activity data on H161 and Q167 support an O_2 binding site within close proximity to these residues.

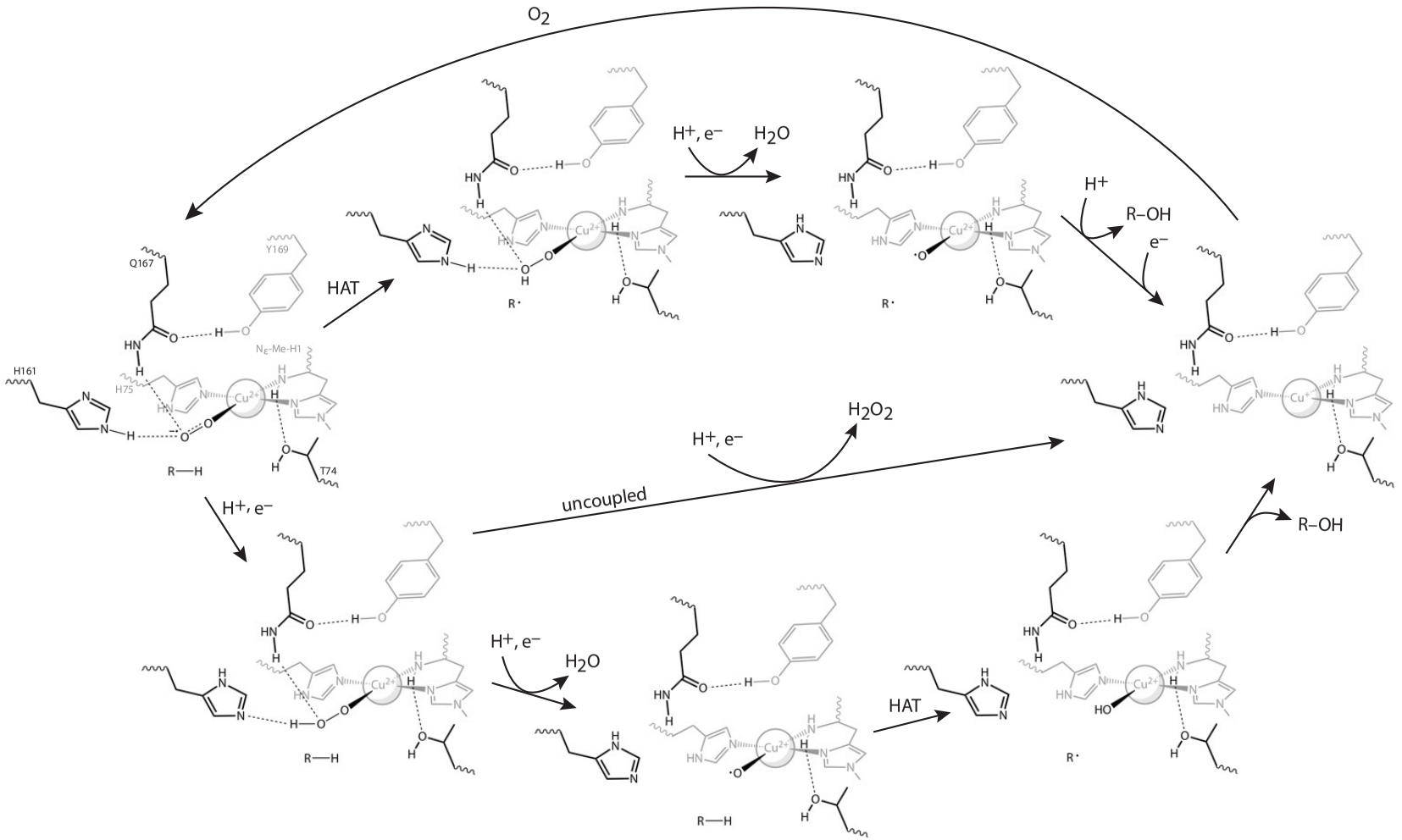

Figure 2.9. **Proposed *Mt*PMO3* reaction mechanisms**. Both begin at left with the generally agreed upon Cu(II)–superoxo species that forms upon O_2 binding to *Mt*PMO3*-Cu(I). The top half follows one possible mechanism based on hydrogen atom transfer (HAT) by the superoxo intermediate, followed by reduction and cleavage of the distal O atom of the hydroperoxo intermediate to form water and an oxyl intermediate that undergoes radical rebound with the substrate. After substrate release, a one-electron reduction returns the Cu(I) enzyme (at right). The bottom half follows a possible mechanism utilizing an oxyl species for HAT, which is formed by reducing and cleaving the terminal O atom of the O_2 adduct to form water. Uncoupling of oxygen activation from substrate hydroxylation could follow the middle pathway that produces peroxide. The release of superoxide from the H161 variants shows that H161 plays a proton transfer role to the Cu(II)-superoxo species, at least in the uncoupled reaction.

The T74A variant exhibits approximately half the O_2 consumption rate of the wild type. It also exhibits about half the product formation of the wild type, when endpoints are taken within the same approximate timescale to obtain initial velocities of O_2 consumption (Figure 2.7). However, T74A forms similar levels of products as the wild type with longer reaction times (Figure 2.10). This may be explained by some turnover-dependent inactivation in the wild type that is abated in T74A, so that while T74A reacts more slowly, its activity is sustained over a longer period of time. The slower initial rate could be attributed to electronic effects from losing the H-bond to the *N*-terminus or some disruption of substrate binding, although the data do not exclude a direct modulation of O_2 binding.

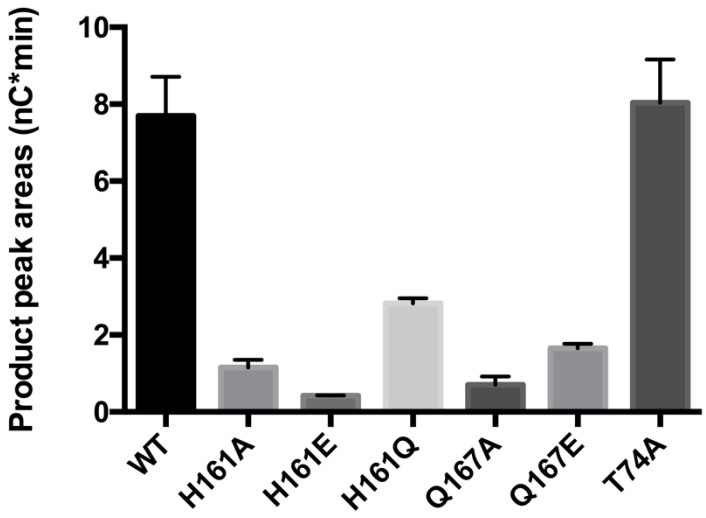

Figure 2.10. Thirty-minute cellulose activity assays with *Mt*PMO3* H-bonding variants. Assays contained 2 µM PMO, 10 mg/mL PASC, atmospheric O_2, and 1 µM *Mt*CDH-2 as the reducing agent. Reactions of 45 µL were carried out in 50 mM sodium acetate buffer (pH 5.0) at 40 ˚C for 30 minutes. Peaks from aldonic acids with DP 5–13 were quantified via HPAEC-PAD. Smaller C1-oxidized products with DP 2–4 were excluded from this analysis, as they are also products of the CDH reaction. (n=3)

EPR Spectroscopy of Variants. X-band EPR spectra of wild type *Mt*PMO3* and the variants described herein show strong Cu(II) signals and indicate efficient loading of Cu into the active site (Figure 2.11). There is also a lack of signal for free Cu(II), showing the proteins as purified are free of excess Cu. All spectra display superhyperfine coupling to multiple ^{14}N nuclei, consistent with Cu(II) binding to the histidine brace motif. The ^{14}N superhyperfine coupling is more resolved in some spectra (*e.g.* H161Q), although this likely reflects small differences in the degree of spectra broadening between the samples (*e.g.* unresolved superhyperfine coupling from other nuclei) rather than significant structural differences. The wild type *Mt*PMO3* EPR spectrum displays a pseudo-axial *g*-tensor that is consistent with the geometry about Cu observed in the crystal structure: an elongated octahedral or square pyramidal geometry that gives rise to an unpaired electron in the $d(x^2–y^2)$ orbital. The fourth equatorial site is presumably occupied by a water ligand; while this is not observed in the crystal structure, likely due to structure resolution or photoreduction of the Cu(II) site to Cu(I) during data collection, the equatorial water ligand has

been observed in Cu(II)-AA10 structures[11]. Similarly, the Y169 –OH ligand is nearly 3 Å away from the Cu center in the crystal structure and may interact more strongly in the Cu(II) oxidation state.

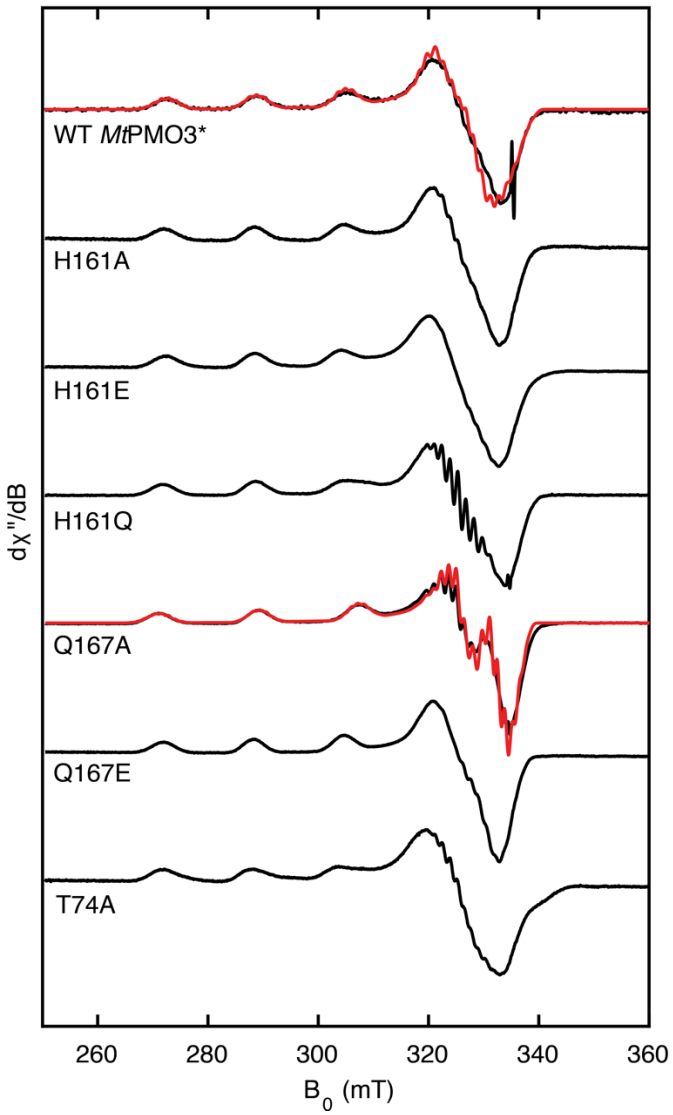

Figure 2.11. X-band EPR spectra of wild type *Mt*PMO3* and six H-bonding network variants. Simulations in red for wilde type (WT) and the Q167A variant. Spectra were recorded at 40 K, 9.4 GHz, 0.2 mW power, and 0.5 mT modulation amplitude and have been scaled for signal strength. The signal ~345 mT in the WT spectra is a feature from the cavity. Simulation parameters for WT *Mt*PMO3*: g = [2.260 2.079 2.032], $A(^{63/65}\text{Cu})$ = [504 30 25] MHz, 3x $A(^{14}\text{N})$ = [40 40 40] MHz, g-strain = [0.007 0.007 0.007]. Simulation parameters for the Q167A variant: g = [2.246 2.055 2.049], $A(^{63/65}\text{Cu})$ = [558 56 20] MHz, 3x $A(^{14}\text{N})$ = [37.6 37.6 37.6] MHz, g-strain = [0.007 0.007 0.007].

The EPR spectra of the H161A and H161E variants are essentially identical to that of wild type *Mt*PMO3*, suggesting that any changes in H-bonding in these variants have little effect on the Cu coordination environment. The EPR spectrum of the Q167A variant exhibits a single g-

tensor (g = [2.246 2.055 2.049]) but one that differs from that of the wild type enzyme (g = [2.260 2.079 2.032]). In particular, the g-tensor is somewhat more axial and has a lower g_1 value (Figure 2.11). We interpret that these spectral changes result from the modification of the H-bonding environment of Y169. As discussed above, Q167 serves as an H-bond acceptor to Y169. With the elimination of this interaction in the Q167A variant, the donor strength of the Y169 –OH ligand to Cu is expected to decrease. As a result, the equatorial ligands are expected to bind Cu more strongly in order to conserve the charge at the Cu site. This raises the $d(x^2–y^2)$ orbital relative to that of the wild type enzyme (Figure 2.12). Because the g_1 value is inversely proportional to the energy difference between the antibonding $d(x^2–y^2)$ orbital and the non-bonding $d(xy)$ orbital[72], the larger energy gap between the $d(x^2–y^2)$ and $d(xy)$ orbitals is expected to result in a modest decrease in the g_1 value for the Q167A variant, as observed experimentally. The Q167E sample serves to test this hypothesis: in the Q167E variant, the H-bond acceptor to the Y169 –OH group is maintained, and the EPR spectrum is restored to that of wild type enzyme, as expected. By enhancing the donor strength of the tyrosyl O ligand in the wild type enzyme, the H-bond between Q167 and Y169 helps to stabilize positive charge buildup on the Cu ion and could aid in the stabilization of high-valent oxyl intermediates.

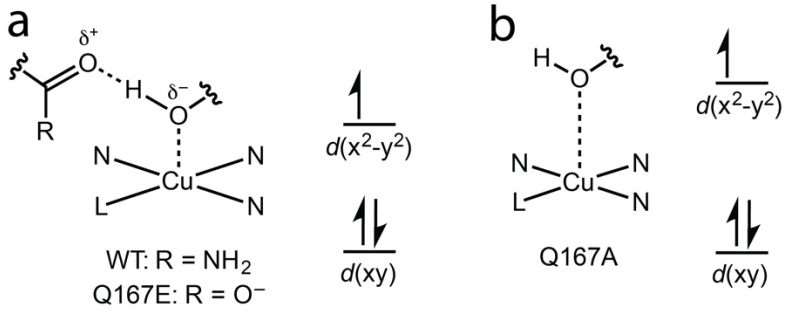

Figure 2.12. Effects of Q167A mutation. (**a**) H-bonding to Y169 in wild type (WT) *Mt*PMO3* and the Q167E variant. (**b**) Geometric and electronic effects of removing a H-bond acceptor to Y169, as in the Q167A variant: elongation of the Cu–Tyr distance and contraction of the Cu–equatorial ligand distances results in an increase in the energy between $d(x^2–y^2)$ and $d(xy)$.

The EPR spectra of the H161Q and T74A variants display a mixture of signals as can be most clearly seen in the broad, asymmetrical shapes of the feature at ~305 mT. This indicates that some subpopulation of the Cu sites in these samples are unaffected by the substitution while others are affected by changes in H-bonding. However, the presence of multiple EPR signals in these samples precludes more detailed, molecular-level analysis.

CONCLUSIONS

Altogether, these data show that the conserved active-site H-bonding network, comprising the secondary sphere histidine and glutamine residues, facilitates O_2 activation in AA9 PMOs. The combined activity data indicate that H161 and Q167 function in O_2 turnover in *Mt*PMO3*, while an additional role in proton transfer to an oxy-bound intermediate may be attributed to H161. These data show that the generation of products is diminished in H161 variants, and instead superoxide is released, therefore suggesting that a Cu(II)–superoxo intermediate is either not

stable in these variants or not the active species in the PMO mechanism. The spectroscopic data show that Q167 enhances the ligand donor strength of the active-site tyrosine, tuning the electronic environment of the Cu center and favoring stabilization of positive charge buildup on the Cu ion. Together, these newly defined roles for H161 and Q167 support the formation of a Cu–oxyl active intermediate. The function of T74 is less clear, but the data demonstrate this residue is less critical for PMO activity. This study provides the first detailed mechanistic insights into the AA9 family of PMOs that play an important role in fungal cellulose degradation and have potential for widespread use in the production of renewable fuels and chemicals.

PREVIOUSLY PUBLISHED MATERIAL

This chapter was modified from a previously published article co-authored by Daniel L. M. Suess, Marc C. Deller, R. David Britt, and Michael A. Marletta. Thanks to the co-authors and publishers at ACS Chemical Biology for allowing use of this material[73].

Data collection:	
Beamline	SSRL 12–2
Wavelength (Å)	0.9795
Space group	$P2_1$
Unit cell dimensions	
a, b, c (Å)	70.94, 134.30, 79.40
α, β, γ (˚)	90.00, 92.92, 90.00
Resolution	48.74–2.45 (2.52–2.45)
Rsym (%)	0.139
I/σ	9.6 (2.0)
No. reflections	50966
Completeness (%)	98.36 (94.74)
Redundancy	4.6 (4.2)

Refinement:	
Rwork/Rfree	0.1626/0.2086 (0.249/0.289)
No. residues	
Protein	1368
Ligand/Ion	6
Water	295
Average B-factor	36.5
RMSD	
bond length	0.011
bond angle	1.379
Ramachandran	
favored (%)	96.7
allowed (%)	2.65
outliers (%)	0.66

Table 2.1. Crystallographic data collection and refinement statistics for *Mt*PMO3*.

CHAPTER THREE: A NEW FAMILY OF PMOS

ABSTRACT

Polysaccharide monooxygenases (PMOs) are copper enzymes secreted by both prokaryotic and eukaryotic microbes that catalyze the oxidative degradation of polysaccharides. Most PMOs described to date act on glycosidic linkages found outside the cell to aid in saprotrophic biomass decomposition. Here we report the discovery of a new family of PMOs found in filamentous ascomycetes that may play a role in fungal cell wall remodeling during hyphal fusion. A representative member of this family from *Neurospora crassa*, *Nc*PMO16b, was homologously expressed in *N. crassa* and purified with copper bound. It produces peroxide *in vitro*; however, its substrate has not yet been identified. *Nc*PMO16b is homologous to HAM-7, a protein previously identified as essential to cell communication and hyphal fusion in *N. crassa.*

INTRODUCTION

Polysaccharide monooxygenases (PMOs) are a growing class of mononuclear copper enzymes that catalyze the degradation of a variety of polysaccharide linkages. They are found in fungi, bacteria, and some viruses. PMOs are secreted proteins; they all have a common beta-sandwich, immunoglobulin-like fold with additional stability conferred by one or more disulfide bonds. Loop features can be rather extended and are thought to vary to accommodate different substrates[46]. The first-discovered and most well-studied family of PMOs are the AA9 enzymes that are part of the cellulolytic machinery in fungi[29]. These PMOs need redox equivalents from their environment and react with oxygen[16,51,73], but they produce peroxide in the absence of substrate[66], and under strongly reducing conditions can utilize peroxide as a co-substrate to oxidize cellulose via hydroxyl radical chemistry[74]. These enzymes have served as a prototype for the characterization of additional families, including AA10[10,18], AA11[12], AA13[19], and the recently characterized xylan-active AA14[75] enzymes. All of these families are hypothesized to be involved in the decomposition of their preferred substrates found in their environments, simply as a way of accessing nutrient sugars.

In recent years, however, a series of discoveries have begun to link PMOs to other physiological processes. *Vibrio cholerae* and *Listeria monocytogenes* AA10 PMOs have been implicated in virulence of these organisms[23–25,41]. Transcript levels of a predicted AA9 PMO in fungal plant pathogen *Magnaporthe oryzae* dramatically increase around the time of infection[76]. Finally, one of the three outlying uncharacterized but predicted PMOs in the *N. crassa* genome has been characterized separately in genetic studies as hyphal anastomosis-7 (*ham-7*), a gene is essential for cell fusion in *N. crassa*[77,78]. Cell fusion, or hyphal anastomosis, is critical at several stages in the growth and development of filamentous fungi, as it permits the passage of water, nutrients, and even nuclei between hyphae in a colony[79]. Without these junctions, a severe growth phenotype is observed. *Neurospora crassa* mutants without *ham-7* (Δ*ham-7* strains) have been observed to be defective in both cell fusion and cell communication, the step that precedes fusion. They exhibit a "flat" condiation phenotype with an altered growth and branching pattern and reduced formation of aerial hyphae[77,80]. They are also female-sterile; formation of female fruiting bodies termed protoperithecia relies on hyphal fusion. Additionally, germlings are observed to neither communicate nor fuse[78].

Herein, we further investigate *ham-7* and a homologous gene (also found in *N. crassa*) with efforts to characterize their biochemical activity and biological function. Given the homology of *ham-7* to other PMOs, its predicted localization to the cell wall, and the phenotype of the Δ*ham-7* strain, we hypothesize that *ham-7* plays a role in remodeling cell wall polysaccharides during hyphal fusion. We term the gene product of *ham-7 Nc*PMO16a and that of its homolog *Nc*PMO16b and suggest calling this new family of PMOs AA16, according to the adopted CAZy nomenclature[17]. Genetic experiments aim to explore whether *Nc*PMO16a might have PMO activity that is relevant to its phenotype, and whether *Nc*PMO16b has any physiological function. Homologous expression of *Nc*PMO16b yields a protein product that is assayed for metal composition, peroxide formation, and substrate preference.

MATERIALS AND METHODS

Strains and Materials. Wild type *Neurospora crassa* (FGSC 2489) as well as deletion strains 13775, 13776, 13937, and 13938 were used in the experiments herein; genomic DNA from *N. crassa* was purified using methods described by the Fungal Genetics Stock Center[60]. Polysaccharide substrates were obtained from Megazyme International and Sigma and treated with Chelex® 100 resin (Bio-Rad) prior to use.

Bioinformatics and Phylogeny Construction. *N. crassa* PMOs were identified as described previously[19], and those belonging to known PMO families were validated against multiple sequence alignment (MSA) datasets previously generated using a Hidden Markov Model-based search algorithm[65,73]. The final validated MSA was fed into PhyML software where bootstrapping analysis was performed[81].

Deletion phenotypes and complementation tests. A double deletion mutant of both *Nc*PMO16a and *Nc*PMO16b was obtained via a cross between the single deletion strains. *Nc*PMO16a complementation strains were constructed using a *his-3* targeting pMF272 vector containing the TEF-1 promoter, CCG-1 terminator, and the NCU00881 gene (amplified from *N. crassa* genomic DNA). For complementation with a mutant allele, a point substitution converting His59 to alanine was introduced using site-directed mutagenesis. The complementation strains were generated by integrating wild type and mutant alleles into the *his-3* locus of a *his-3*; Δ*ham-7* strain.

To observe phenotypes of the *Nc*PMO14a complementation strains and the *Nc*PMO16b deletion mutant, all strains were grown in slants on Vogel's minimal media with sucrose for 7 days (2 days at 30 ˚C in the dark followed by 5 days at 23 ˚C on the bench). A conidial suspension from each strain was made with water, filtered with cheesecloth, and diluted to 2.5×10^6 cells/mL. These suspensions (20 µL of each) were used to inoculate the center of large (14.2 cm) Petri dishes, which were grown for 2 days at 30 ˚C with measurement of colony diameter at indicated time points.

Protein Expression and Purification. *Nc*PMO16b was expressed in *Neurospora crassa* using a knock-in expression method, as previously described[61]. A point substitution was introduced using site-directed mutagenesis to a pCSR-1 vector containing wild type *Nc*PMO16b (gene ID NCU02884, isolated from *N. crassa* genomic DNA) to truncate the transcript before the predicted site of GPI attachment. The construct was transformed into *E. coli* DH5α cells for propagation, and sequence-validated linearized target DNA constructs were transformed into *N. crassa* for expression. The same was performed for *Nc*PMO16a (gene ID NCU00881). *Nc*PMO16b was purified from the *N.*

crassa secretome as described for previous PMOs[37]. Before the final gel filtration step, the enzyme was reconstituted with excess $CuSO_4$ at pH 5.0 for 4 hours at ambient temperature. The final chromatography step also functioned to desalt the sample of excess $CuSO_4$. Metal analysis was performed on a Thermo Fisher iCAP Qc ICP-MS using an internal gallium standard. All buffers used in this study were prepared using >18 MΩ water and did not have detectable iron, nickel, copper, or zinc by ICP-MS.

Peroxide Formation Assays. Horseradish peroxidase (HRP)-coupled assays were based on previously described methods[66], utilizing Amplex Red as a substrate for the photometric detection of peroxide in *Nc*PMO16b reactions over time. Assays contained 100 µL of 100 mM HEPES (pH 7.0), 0.5 µM *Nc*PMO16b, 0.5 U/mL HRP, 50 µM Amplex Red, and 50 µM ascorbate. Reactions were carried out in flat-bottom, untreated 96-well plates (Corning), and detection at 573 nm was performed with a SpectraMax 340 plate reader (Molecular Devices) and analyzed with SoftMax Pro software.

Substrate Activity Assays. *Nc*PMO16b (5 µM) was mixed with 10 mg/mL polysaccharide substrate and 2 mM ascorbate with atmospheric O_2. Reactions of 60 µL were carried out in 50 mM sodium acetate buffer (pH 5.0) at 30 ˚C for 1–4 hours. Assay products were analyzed via HPAEC-PAD as described previously[16]. For ESI-MS analysis, assay products were diluted ten-fold in Milli-Q ultrapure water after addition of an equal volume of 0.2 M NaOH (as used normally to quench the reaction).

Removal of copper to make apo *Nc*PMO16b. EDTA was insufficient for the removal of Cu(II) from *Nc*PMO16b. To make the apo enzyme, the sample (100 µM *Nc*PMO16b in 100 mM sodium acetate pH 5.0, 150 mM NaCl) was degassed (headspace only) and brought into an anaerobic environment to equilibrate overnight prior to reduction with 4 mM ascorbate for 15 minutes. The removal of Cu(I) was performed by addition of 2 mM bathocuproine sulphonate (BCS) from a 100 mM stock for 5 minutes. Formation of the BCS-Cu(I) complex was measured by absorbance at 483 nm using ε = 13 $mM^{-1}cm^{-1}$. The sample was then desalted into the original buffer using a PD MiniTrap desalting column (GE Life Sciences), removed to ambient O_2, and concentrated using a 3,000 kDa-cutoff centrifugal filter.

RESULTS AND DISCUSSION

Phylogeny of *N. crassa* PMOs and proposed new PMO family. Of the 20 PMOs predicted in the *N. crassa* genome, three remain uncharacterized or in separate clades from characterized PMOs (Figure 3.1). As each clade so far has defined a distinct PMO family (distinguished by activity towards a distinct substrate), these three predicted PMOs are considered to reside in new families with unknown substrates. This work terms genes NCU00881 and NCU02884 members of a new family, PMO16. These gene products (*Nc*PMO16a and *Nc*PMO16b, respectively) are predicted to be heavily glycosylated and GPI-anchored, and as such tethered to the cell wall. No other PMOs to date have been known to localize to the cell wall; they have all been found in the secretome.

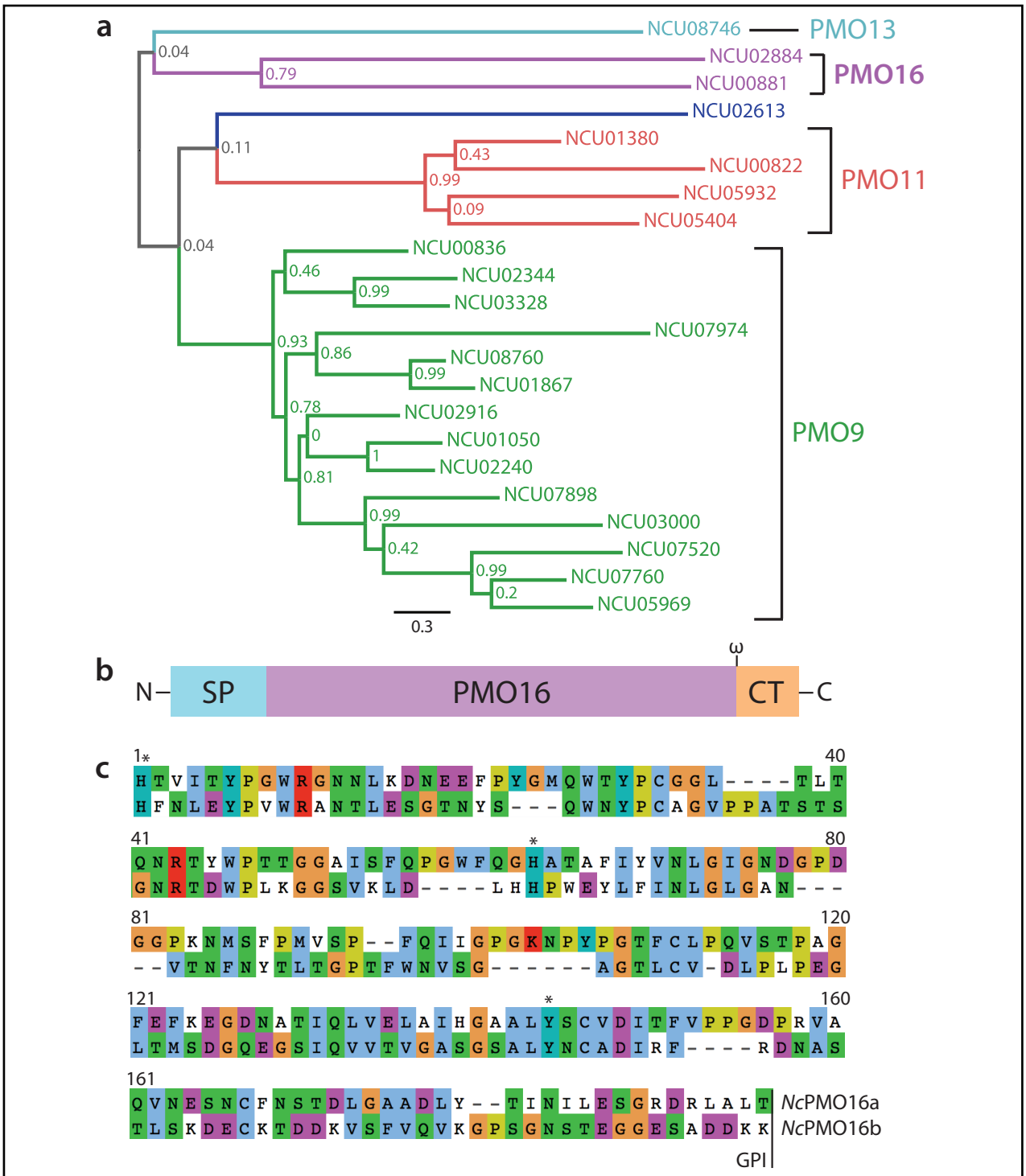

Figure 3.1. Family PMO16. (**a**) Phylogenetic tree of all 20 predicted or characterized PMOs in *N. crassa*. The PMO16 family (termed herein) are as yet uncharacterized. Node numbers are bootstrap confidence values. (**b**) Schematic of PMO16 domain architecture, flanked by a secretion signal peptide (SP) and C-terminal sequence (CT) that is cleaved during GPI anchor addition at the ω site. (**c**) Pairwise sequence alignment of the two PMO16s from *N. crassa*. Sequence identity is 25%, similarity 47%. Conserved active-site residues are marked (*).

Phenotypes of strains carrying a *Nc*PMO16b deletion or a *Nc*PMO16a mutant allele. The *Nc*PMO16b deletion strain has no observable growth phenotype under laboratory growth conditions (minimal medium plus sucrose) (Figure 3.2). This PMO may not be transcribed as highly as *Nc*PMO16a and may not serve the same role in cell fusion.

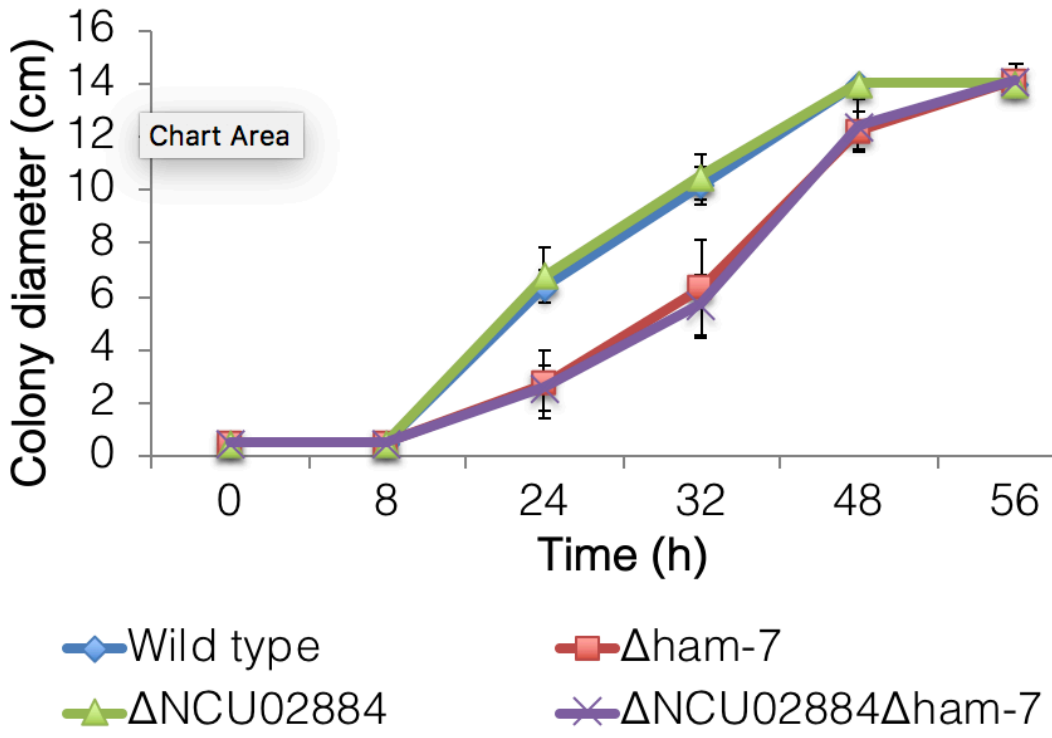

Figure 3.2. The *Nc*PMO16b deletion mutant has no observable phenotype. The *Nc*PMO16b deletion strain grows like wild type *N. crassa* under the conditions tested, whereas the double deletion strain grows like the *Nc*PMO16a single deletion. The plate diameter is 14.2 cm. NCU02884 = *Nc*PMO16b; ham-7 = *Nc*PMO16a.

Complementation of the *Nc*PMO16a deletion with wild type *Nc*PMO16a restores wild type growth, whereas complementation with the H59A mutant allele does not (Figure 3.3). The H59A mutation (mature peptide numbering) is expected to disrupt the copper binding site, rendering the PMO inactive. The strain with the mutant allele grows similarly to the deletion strain, suggesting PMO activity is relevant to the physiological function of *Nc*PMO16a. The complemented genes are under the strong constitutive TEF-1 promoter.

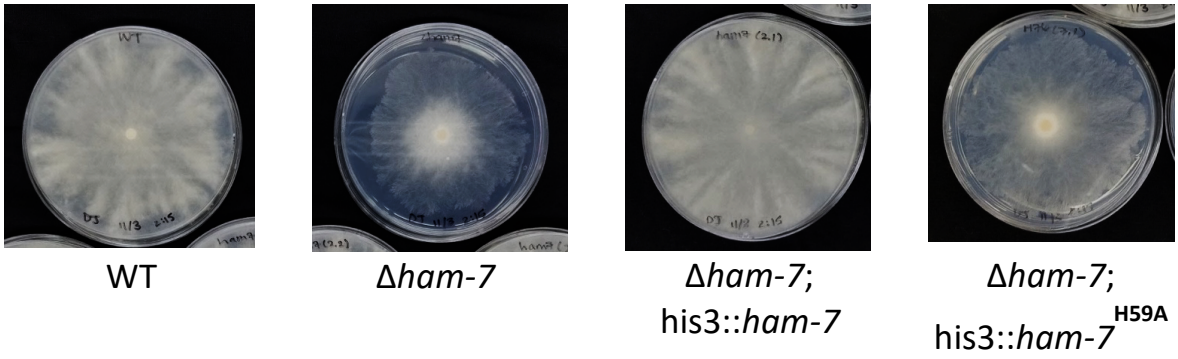

Figure 3.3. *Nc*PMO16a catalytic site is necessary for wild type growth. Complementation with wild type *Nc*PMO16a (*ham-7*) at the his3 locus restores wild type growth of the deletion strain; however, complementation with a mutant allele that is expected to disrupt active site copper binding does not restore wild type growth.

Expression and characterization of *Nc*PMO16b. Overexpression of *Nc*PMO16b truncated at the ω site in *N. crassa* was obtained via insertion at the *csr-1* locus and regulated under the GAP-5 promoter (Figure 3.4). Identical methods failed to produce *Nc*PMO16a. *Nc*PMO16b was purified from the secretome and appears heavily glycosylated based on appearance as a diffuse band at high molecular weight via SDS-PAGE.

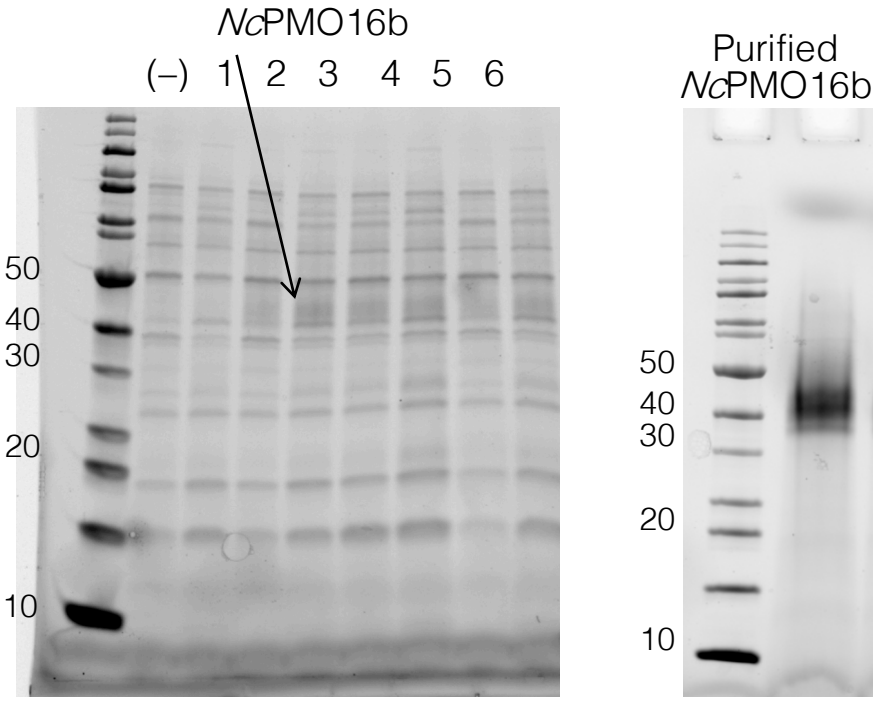

Figure 3.4. Expression and purification of *Nc*PMO16b. SDS-PAGE analysis of secretome samples from wild type *N. crassa* (–) and seven *Nc*PMO16b transformants (left). Transformant #3 was chosen for large-scale expression and purification (right). Molecular weight markers (kDa) at left of gel images.

ICP-MS analysis shows *Nc*PMO16b contains copper in a molar ratio of approximately 1:1 (Figure 3.5). There is also a non-trivial amount of zinc in the sample, present as a contaminant.

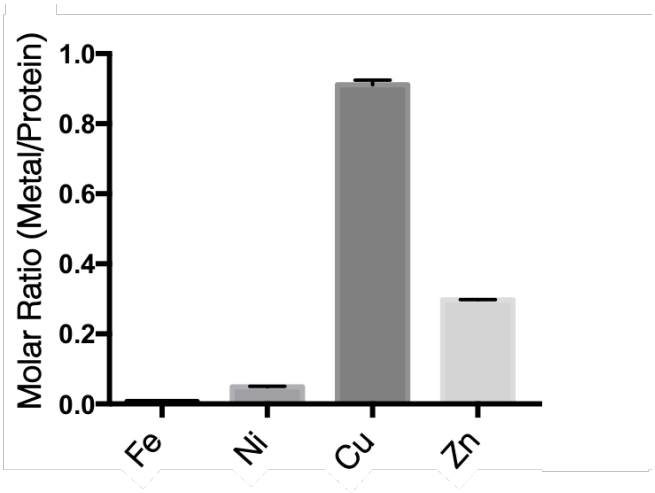

Figure 3.5. *Nc*PMO16b contains copper as purified. ICP-MS analysis of *Nc*PMO16b. Error bars indicate standard deviation. (n=3)

Peroxide formation by *Nc*PMO16b. Another defining feature of PMOs is that in the absence of substrate they will uncouple oxygen reduction from substrate oxidation, resulting in the reduction of O_2 to peroxide. *Nc*PMO16b produces peroxide in the absence of substrate, indicating biochemical behavior of a PMO (Figure 3.6).

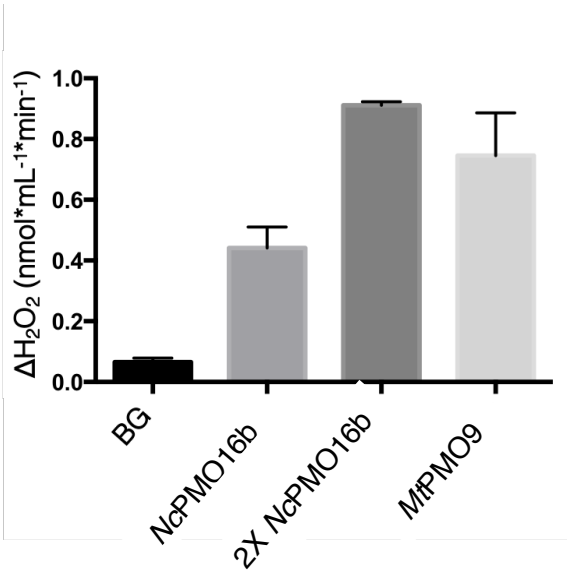

Figure 3.6. *Nc*PMO16b produces peroxide in a concentration-dependent manner. Horseradish peroxidase (HRP)-coupled assays were carried out in 100 µL of 100 mM HEPES pH 7.0 and contained 0.5 µM PMO (1 µM where specified "2X"), 0.5 U/mL HRP, 50 µM Amplex Red, 50 µM ascorbate, and ambient O_2. BG = background, without PMO. *Mt*PMO9 serves as a positive control. Error bars indicate standard deviation. (n=3)

Substrate activity assays. *Nc*PMO16b does not appear to exhibit monooxygenase activity toward any substrate tested thus far. A complete list of substrates tested follows: xylan, xyloglucan, β-glucan (barley), lichenan, mannan, glucomannan, galactomannan, chitosan, α- and β-chitin, phosphoric acid-swollen cellulose (PASC), cellohexaose, pachyman, curdlan, yeast β-glucan, and laminarin. With laminarin, multiple new peaks with earlier retention times appear in the HPAEC-PAD chromatogram after *Nc*PMO16b treatment (Figure 3.7), and a small percentage of oxidized oligosaccharides appear by ESI-MS (Table 3.1). Other β-1,3-glucans tested (pachyman, curdlan, yeast β-glucan) did not appear to be substrates. Laminarin (Sigma) was the only soluble substrate tested with an average degree of polymerization (DP) of 25[82], and thus the lack of observable activity on the other β-1,3-glucans was attributed to a putative preference for shorter or more soluble substrates (although most PMOs to date prefer insoluble substrates). Overall, this led to the initial observation that laminarin might be a substrate for *Nc*PMO16b.

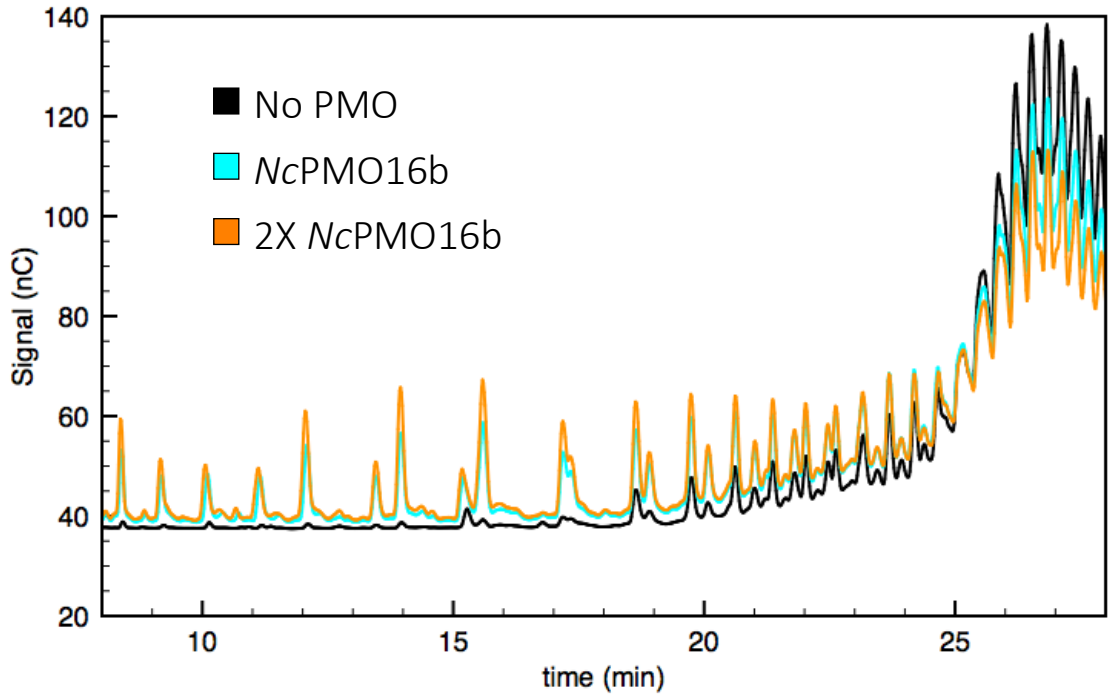

Figure 3.7. HPAEC-PAD analysis of laminarin assays. Smaller products appear at shorter retention times in the reactions with *Nc*PMO16b. Assays were carried out in 60 µL of 50 µM sodium acetate (pH 5.0) with 5 mg/mL laminarin, 2 mM ascorbate, and 2.5 µM *Nc*PMO16b (5 µM for "2X") for 4h at 30 ˚C.

Compound [M]	Chemical Formula	Adducts Detected	*Nc*PMO16b	–PMO	Apo	Apo +Cu
$G1_{ox}$	$C_6H_{10}O_6$	$[M+Na]^+$	0.3	-	-	0.2
$G2_{ox}$	$C_{12}H_{20}O_{11}$	$[M+Na]^+$	0.3	-	-	0.2
$G3_{ox}H_2O$	$C_{18}H_{32}O_{17}$	$[M+Na]^+$	0.2	-	-	0.1
$G4_{ox}$	$C_{24}H_{40}O_{21}$	$[M+Na]^+$	0.1	-	-	0.2
$G4_{ox}H_2O$	$C_{24}H_{42}O_{22}$	$[M+Na]^+$	0.3	-	-	0.2
$G5_{ox}H_2O$	$C_{30}H_{52}O_{27}$	$[M+Na]^+$	0.1	-	-	0.1

Table 3.1. Relative percent abundances of oxidized glucose oligomers from laminarin reactions. Total ion count for each sample included all detectable glucan ions with DP=1–5, both oxidized and non-oxidized species. Low percent abundances of oxidized species are attributed to the large amounts of non-oxidized glucans that are components of the substrate mixture. Oxidized products were <LOD in assays without PMO and with apo-PMO (S/N cutoff = 4). Addition of Cu(II) rescues activity and demonstrates that the copper cofactor is required for catalysis.

However, the negative controls did not fit this observation; specifically, the reaction without ascorbate repeatedly produced HPAEC-PAD traces identical to those of the complete reaction (Figure 3.8).

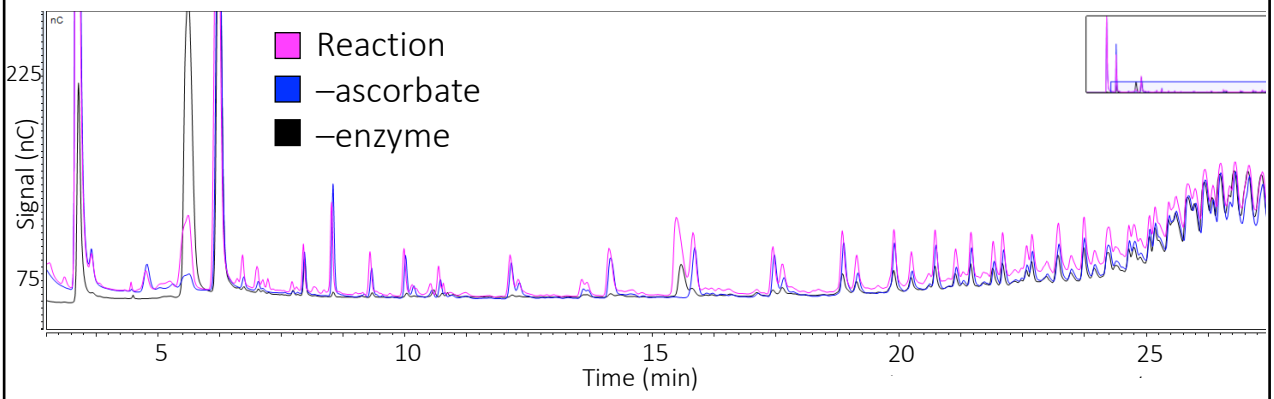

Figure 3.8. Reductant independence of *Nc*PMO16b reactions on laminarin. The HPAEC-PAD traces, especially the smaller peaks at shorter retention times (~7–18 min) observed with *Nc*PMO16b treatment (magenta), appear nearly identical to those of the control lacking ascorbate (blue). Assays were carried out in 60 µL of 50 µM sodium acetate (pH 5.0) with 5 mg/mL laminarin, 750 µM ascorbate, and 5 µM *Nc*PMO16b for 1h at 30 ˚C.

The purified *Nc*PMO16b sample was digested with trypsin and sent for peptide analysis via LC-MS, which confirmed broad contamination by a number of other *N. crassa* enzymes, including multiple peptides for a β-1,3-glucanase (Table 3.2). This explained why enzyme treatment of laminarin (a β-1,3-glucan) consistently generated new smaller products observed via HPAEC-PAD and ESI-MS.

Description	# Peptides
NCU07523 | Neurospora crassa OR74A 1,3-beta glucanase (948 aa)	27
NCU06512 | Neurospora crassa OR74A methionine-8 (770 aa)	26
NCU08909 | Neurospora crassa OR74A beta-1,3-glucanosyltransferase (543 aa)	19
NCU11356 | Neurospora crassa OR74A phenazine biosynthesis PhzC/PhzF protein (339 aa)	16
NCU10042 | Neurospora crassa OR74A embden-meyerhof pathway-7 (439 aa)	15
NCU04883 | Neurospora crassa OR74A glycosyl hydrolase family 18-4 (486 aa)	15
NCU07281 | Neurospora crassa OR74A glucose-6-phosphate isomerase (562 aa)	13
NCU04194 | Neurospora crassa OR74A hypothetical protein (573 aa)	13
NCU02136 | Neurospora crassa OR74A transaldolase (325 aa)	12
NCU09560 | Neurospora crassa OR74A superoxide dismutase (229 aa)	10
NCU07253 | Neurospora crassa OR74A 1,3-beta-glucanosyltransferase gel1 (467 aa)	9
NCU02884 | Neurospora crassa OR74A hypothetical protein (221 aa)	9
NCU08936 | Neurospora crassa OR74A clock-controlled gene-15 (412 aa)	8
NCU06781 | Neurospora crassa OR74A 1,3-beta-glucanosyltransferase Gel2 (495 aa)	7
NCU04643 | Neurospora crassa OR74A peptide-N4-(N-acetyl-beta-glucosaminyl)asparagine amidase A (822 aa)	7
NCU04430 | Neurospora crassa OR74A leupeptin-inactivating enzyme 1 (509 aa)	6
NCU08549 | Neurospora crassa OR74A UDP-galactose 4-epimerase (286 aa)	4
NCU03530 | Neurospora crassa OR74A anchored cell wall protein-6 (261 aa)	3
NCU01821 | Neurospora crassa OR74A alanine-glyoxylate aminotransferase (447 aa)	3
NCU04108 | Neurospora crassa OR74A isoamyl alcohol oxidase (568 aa)	2
NCU10641 | Neurospora crassa OR74A hypothetical protein (191 aa)	2
NCU06850 | Neurospora crassa OR74A 1,3-beta-glucanosyltransferase gel3 (431 aa)	2
NCU08720 | Neurospora crassa OR74A hypothetical protein (181 aa)	1
NCU02252 | Neurospora crassa OR74A embden-meyerhof pathway-6 (520 aa)	1
NCU06811 | Neurospora crassa OR74A hypothetical protein (387 aa)	1

Table 3.2. Peptides in *Nc*PMO16b as purified. Peptides in the purified, digested *Nc*PMO16b sample found from searching a database of all *N. crassa* proteins. The contaminating hydrolase (NCU07523) as well as the target construct (NCU02884, *Nc*PMO16b) are in bold text.

The question of why oxidized products were observable via ESI-MS was answered as well. All oxidized sugars disappear with addition of an equimolar ratio of horseradish peroxidase and an excess of its substrate Amplex Red, indicating that oxidation is not a result of monooxygenase activity (Table 3.3). Hydrogen peroxide is known to readily convert glucose to gluconic acid by oxidizing the hemiacetal hydroxyl to a carboxyl group; it is very likely that the peroxide made by *Nc*PMO16b during the course of incubation with laminarin oxidized the reducing ends of laminarodextrins either already present in solution or produced via hydrolysis activity of the contaminating glucanase.

Compound [M]	Chemical Formula	Adducts Detected	Reaction	–ascorbate	Reaction +HRP
G1	$C_6H_{12}O_6$	$[M+Na]^+$	6636937	6184244	4911774
G2	$C_{12}H_{22}O_{11}$	$[M+Na]^+$	170444	168128	271812
G3	$C_{18}H_{32}O_{16}$	$[M+Na]^+$	287958	390026	1082417
G4	$C_{24}H_{42}O_{21}$	$[M+Na]^+$	307209	249674	363713
G5	$C_{30}H_{52}O_{26}$	$[M+Na]^+$	324666	64181	400700
G6	$C_{36}H_{62}O_{31}$	$[M+Na]^+$	nd	25065	339084
$G1_{ox}$	$C_6H_{10}O_6$	$[M+Na]^+$	52031	2827	nd
$G2_{ox}$	$C_{12}H_{20}O_{11}$	$[M+Na]^+$	nd	nd	nd
$G3_{ox}$	$C_{18}H_{30}O_{16}$	$[M+Na]^+$	nd	nd	nd
$G4_{ox}$	$C_{24}H_{40}O_{21}$	$[M+Na]^+$	nd	nd	nd
$G5_{ox}$	$C_{30}H_{50}O_{26}$	$[M+Na]^+$	nd	nd	nd
$G6_{ox}$	$C_{36}H_{60}O_{31}$	$[M+Na]^+$	nd	nd	nd
$G1_{ox}H_2O$	$C_6H_{12}O_7$	$[M+Na]^+$	4459	nd	nd
$G2_{ox}H_2O$	$C_{12}H_{22}O_{12}$	$[M+Na]^+$	2732	nd	nd
$G3_{ox}H_2O$	$C_{18}H_{32}O_{17}$	$[M+Na]^+$	nd	nd	nd
$G4_{ox}H_2O$	$C_{24}H_{42}O_{22}$	$[M+Na]^+$	8959	nd	nd
$G5_{ox}H_2O$	$C_{30}H_{52}O_{27}$	$[M+Na]^+$	4883	nd	nd
$G6_{ox}H_2O$	$C_{36}H_{62}O_{32}$	$[M+Na]^+$	6099	nd	nd

Table 3.3. Addition of HRP to assays eliminates oxidized products observed via ESI-MS. Raw ion counts of predicted *Nc*PMO16b products, degree of polymerization 1–6, both nonoxidized (*i.e.* G1) and oxidized (*i.e.* $G1_{ox}$ or hydrated product $G1_{ox}H_2O$). nd = not detected. S/N cutoff = 4.0.

CONCLUSIONS

Further work is needed to characterize the biochemical activity of the PMO16 family. It is possible that additional assays need to be developed to screen for PMO16 activity or substrate preferences. A structure of a PMO16 will add to the field, as these PMOs vary significantly from other structurally characterized PMOs to the extent that homology models cannot be built using standard methodologies. Since there is some evidence that peroxide or reactive oxygen species generally are implicated in hyphal communication and fusion, additional genetics studies including germling fusion assays on *Nc*PMO16a varying peroxide or peroxide scavengers may be informative. Finally, there is the question of the relatedness of *Nc*PMO16a and *Nc*PMO16b: since *Nc*PMO16a is the protein with clear physiological relevance, its expression and characterization are of utmost importance.

PERMISSION TO USE DATA

Many thanks to collaborators Pedro Gonçalves and Darae Jun in the Glass laboratory for allowing use of the *N. crassa* genetics data.

CHAPTER FOUR: CONCLUSION AND OUTLOOK

The initial discovery of cellulose-active fungal PMOs laid the groundwork for the PMO field, which is actively growing. Elucidation of the PMO mechanism will be a major milestone. Defining the contributions of the secondary coordinating residues towards O_2 activation was informative, but studies employing soluble substrates and controlled turnover are needed to discern which intermediate is responsible for hydrogen atom abstraction from the substrate. Most copper monooxygenases utilize Cu(II)–superoxo, and the formation of Cu(III)–oxyl is heavily disputed (although it could theoretically be stabilized in fungal PMOs by an axial tyrosyl radical). However, the higher C–H bond dissociation energies at glycosidic linkages may require a stronger oxidant than a superoxo species. There is a difference in electron stoichiometry between the superoxo and oxyl pathways that could perhaps be leveraged to discern between the two.

The last five years in the PMO field have been filled with new discoveries, particularly of new families acting on novel substrates. The characterization of the family here termed PMO16 will enable the growth of the field in completely new directions. It is possible that the precedent of PMO action in biomass degradation is limiting what we can discover about new PMO biochemistry by biasing the assay methodology. In particular, it is possible that the difficulty finding the substrate for *Nc*PMO16b is due to use of assays previously developed for biomass-degrading PMOs, which invoke the testing of heterogeneous substrates as well as detection methods for heterogeneous products with a range of DP. It could be that the physiology of cell fusion requires a PMO that acts on one specific substrate or produces one specific product.

Gene duplication is largely prevented in *N. crassa* by a genome defense mechanism termed RIP[83], so the existence of both *Nc*PMO16a and *Nc*PMO16b with shared sequence identity of only 25% may indicate slightly different activities for each. There are multiple PMO9s in *N. crassa* that act on cellulose, but further investigation has shown a number of these enzymes to have a greater degree of substrate tolerance for short-chain cellodextrins or various hemicelluloses. Since *Nc*PMO16b has no relevant phenotype, it may be better to focus on *Nc*PMO16a expression and characterization. Overexpression of the *Nc*PMO16a truncation could be making the native host sick, and therefore it may be advisable to attempt expression in another host such as *Pichia pastoris*. Alternatively it may be sufficient to express *Nc*PMO16a orthologs in *N. crassa*: direct orthologs are present in other filamentous fungi including SymB (*Epichloe festuchae*) and IDC2 (*Podospora anserina*) that produce the same phenotype as *Nc*PMO16a (HAM-7)[84,85]. More distant *Nc*PMO16a homologs appear in the genomes of opportunistic fungal pathogens, for example in *Cryptococcus* spp., and could be highly relevant drug targets.

Aside from the two PMO16 enzymes, there is one remaining predicted PMO in *N. crassa* that does not cluster phylogenetically with the others, corresponding to gene ID NCU02613. Nothing is known about this protein except that it shows substantial downregulation of expression (alongside *ham-7*) in the Δ*pp-1* mutant[78].

Efforts to characterize of the remaining PMOs in *N. crassa*, combined with imminent discoveries about PMOs in pathogens, indicate that the PMO field is poised for explosive growth. Discoveries that shift the landscape of the PMO field can be expected in the coming years, generating new knowledge that will be applicable in multiple areas spanning biomass deconstruction, antibiotic discovery, and agricultural science.

REFERENCES

1. Vaaje-Kolstad, G., Horn, S. J., van Aalten, D. M. F., Synstad, B. & Eijsink, V. G. H. The Non-catalytic Chitin-binding Protein CBP21 from Serratia marcescens Is Essential for Chitin Degradation. *J. Biol. Chem.* **280,** 28492–28497 (2005).
2. Karkehabadi, S. *et al.* The First Structure of a Glycoside Hydrolase Family 61 Member, Cel61B from Hypocrea jecorina, at 1.6 Å Resolution. *J. Mol. Biol.* **383,** 144–154 (2008).
3. Harris, P. V *et al.* Stimulation of Lignocellulosic Biomass Hydrolysis by Proteins of Glycoside Hydrolase Family 61: Structure and Function of a Large, Enigmatic Family. *Biochemistry* **49,** 3305–3316 (2010).
4. Quinlan, R. J. *et al.* Insights into the oxidative degradation of cellulose by a copper metalloenzyme that exploits biomass components. *Proc. Natl. Acad. Sci. USA* **108,** 15079–15084 (2011).
5. Aachmann, F. L., Sørlie, M., Skjåk-Bræk, G., Eijsink, V. G. H. & Vaaje-Kolstad, G. NMR structure of a lytic polysaccharide monooxygenase provides insight into copper binding, protein dynamics, and substrate interactions. *Proc. Natl. Acad. Sci. USA* **109,** 18779–18784 (2012).
6. Vaaje-Kolstad, G. *et al.* Characterization of the Chitinolytic Machinery of Enterococcus faecalis V583 and High-Resolution Structure of Its Oxidative CBM33 Enzyme. *J. Mol. Biol.* **416,** 239–254 (2012).
7. Li, X., Beeson, W. T., Phillips, C. M., Marletta, M. A. & Cate, J. H. D. Structural Basis for Substrate Targeting and Catalysis by Fungal Polysaccharide Monooxygenases. *Structure* **20,** 1051–1061 (2012).
8. Wu, M. *et al.* Crystal Structure and Computational Characterization of the Lytic Polysaccharide Monooxygenase GH61D from the Basidiomycota Fungus Phanerochaete chrysosporium. *J. Biol. Chem.* **288,** 12828–12839 (2013).
9. Hemsworth, G. R. *et al.* The Copper Active Site of CBM33 Polysaccharide Oxygenases. *J. Am. Chem. Soc.* **135,** 6069–6077 (2013).
10. Forsberg, Z. *et al.* Structural and functional characterization of a conserved pair of bacterial cellulose-oxidizing lytic polysaccharide monooxygenases. *Proc. Natl. Acad. Sci. USA* **111,** 8446–8451 (2014).
11. Gudmundsson, M. *et al.* Structural and Electronic Snapshots during the Transition from a Cu(II) to Cu(I) Metal Center of a Lytic Polysaccharide Monooxygenase by X-ray Photoreduction. *J. Biol. Chem.* **289,** 18782–18792 (2014).
12. Hemsworth, G. R., Henrissat, B., Davies, G. J. & Walton, P. H. Discovery and characterization of a new family of lytic polysaccharide monooxygenases. *Nat. Chem. Biol.* **10,** 122–126 (2014).
13. Lo Leggio, L. *et al.* Structure and boosting activity of a starch-degrading lytic polysaccharide monooxygenase. *Nat Commun* **6,** 5961 (2015).
14. Borisova, A. S. *et al.* Structural and functional characterization of a lytic polysaccharide monooxygenase with broad substrate specificity. *J Biol Chem* **290,** 22955–22969 (2015).
15. Chiu, E. *et al.* Structural basis for the enhancement of virulence by viral spindles and their in vivo crystallization. *Proc Natl Acad Sci U S A* **112,** 3973–3978 (2015).
16. Phillips, C. M., Beeson, W. T., Cate, J. H. D. & Marletta, M. A. Cellobiose Dehydrogenase

and a Copper-Dependent Polysaccharide Monooxygenase Potentiate Cellulose Degradation by Neurospora crassa. *ACS Chem. Biol.* **6,** 1399–1406 (2011).
17. Levasseur, A., Drula, E., Lombard, V., Coutinho, P. & Henrissat, B. Expansion of the enzymatic repertoire of the CAZy database to integrate auxiliary redox enzymes. *Biotechnol. Biofuels* **6,** 41–54 (2013).
18. Forsberg, Z. *et al.* Comparative Study of Two Chitin-Active and Two Cellulose-Active AA10-Type Lytic Polysaccharide Monooxygenases. *Biochemistry* **53,** 1647–1656 (2014).
19. Vu, V. V., Beeson, W. T., Span, E. A., Farquhar, E. R. & Marletta, M. A. A family of starch-active polysaccharide monooxygenases. *Proc. Natl. Acad. Sci. U. S. A.* **111,** (2014).
20. Agger, J. W. *et al.* Discovery of LPMO activity on hemicelluloses shows the importance of oxidative processes in plant cell wall degradation. *Proc. Natl. Acad. Sci. USA* **111,** 6287–6292 (2014).
21. Bennati-Granier, C. *et al.* Substrate specificity and regioselectivity of fungal AA9 lytic polysaccharide monooxygenases secreted by Podospora anserina. *Biotechnol Biofuels* **8,** 90 (2015).
22. Bhowmick, R. *et al.* Intestinal adherence of Vibrio cholerae involves a coordinated interaction between colonization factor GbpA and mucin. *Infect Immun* **76,** 4968–4977 (2008).
23. Chaudhuri, S. *et al.* Contribution of chitinases to Listeria monocytogenes pathogenesis. *Appl Env. Microbiol* **76,** 7302–7305 (2010).
24. Loose, J. S., Forsberg, Z., Fraaije, M. W., Eijsink, V. G. & Vaaje-Kolstad, G. A rapid quantitative activity assay shows that the Vibrio cholerae colonization factor GbpA is an active lytic polysaccharide monooxygenase. *FEBS Lett* **588,** 3435–3440 (2014).
25. Paspaliari, D. K., Loose, J. S., Larsen, M. H. & Vaaje-Kolstad, G. Listeria monocytogenes has a functional chitinolytic system and an active lytic polysaccharide monooxygenase. *FEBS J* (2015). doi:10.1111/febs.13191
26. Frederiksen, R. F. *et al.* Bacterial chitinases and chitin-binding proteins as virulence factors. *Microbiology* **159,** 833–847 (2013).
27. Takemoto, Y., Mitsuhashi, W., Murakami, R., Konishi, H. & Miyamoto, K. The N-terminal region of an entomopoxvirus fusolin is essential for the enhancement of peroral infection, whereas the C-terminal region is eliminated in digestive juice. *J Virol* **82,** 12406–12415 (2008).
28. Li, Z. *et al.* Characterization of a chitin-binding protein GP37 of Spodoptera litura multicapsid nucleopolyhedrovirus. *Virus Res* **96,** 113–122 (2003).
29. Beeson, W. T., Vu, V. V., Span, E. A., Phillips, C. M. & Marletta, M. A. *Cellulose degradation by polysaccharide monooxygenases*. *Annual Review of Biochemistry* **84,** (2015).
30. Book, A. J. *et al.* Evolution of substrate specificity in bacterial AA10 lytic polysaccharide monooxygenases. *Biotechnol Biofuels* **7,** 109 (2014).
31. Bruto, M., Prigent-Combaret, C., Luis, P., Moenne-Loccoz, Y. & Muller, D. Frequent, independent transfers of a catabolic gene from bacteria to contrasted filamentous eukaryotes. *Proc Biol Sci* **281,** 20140848 (2014).
32. Bork, P., Holm, L. & Sander, C. The immunoglobulin fold. Structural classification, sequence patterns and common core. *J Mol Biol* **242,** 309–320 (1994).
33. Jee, J. G. *et al.* Solution structure of the fibronectin type III domain from Bacillus circulans

WL-12 chitinase A1. *J Biol Chem* **277,** 1388–1397 (2002).
34. Alahuhta, M. *et al.* Structure of a fibronectin type III-like module from Clostridium thermocellum. *Acta Crystallogr Sect F Struct Biol Cryst Commun* **66,** 878–880 (2010).
35. Nakagawa, Y. S. *et al.* A small lytic polysaccharide monooxygenase from Streptomyces griseus targeting alpha- and beta-chitin. *FEBS J* **282,** 1065–1079 (2015).
36. Frandsen, K. E. *et al.* The molecular basis of polysaccharide cleavage by lytic polysaccharide monooxygenases. *Nat Chem Biol* **12,** 298–303 (2016).
37. Vu, V. V, Beeson, W. T., Phillips, C. M., Cate, J. H. & Marletta, M. A. Determinants of regioselective hydroxylation in the fungal polysaccharide monooxygenases. *J. Am. Chem. Soc.* **136,** 562–565 (2014).
38. Hemsworth, G. R., Davies, G. J. & Walton, P. H. Recent insights into copper-containing lytic polysaccharide mono-oxygenases. *Curr. Opin. Chem. Biol.* **23,** 660–668 (2013).
39. Blanksby, S. J. & Ellison, G. B. Bond Dissociation Energies of Organic Molecules. *Acc. Chem. Res.* **36,** 255–263 (2003).
40. Taylor, C. B. *et al.* Computational investigation of glycosylation effects on a family 1 carbohydrate-binding module. *J. Biol. Chem.* **287,** 3147–3155 (2012).
41. Wong, E. *et al.* The Vibrio cholerae colonization factor GbpA possesses a modular structure that governs binding to different host surfaces. *PLoS Pathog* **8,** e1002373 (2012).
42. Zhang, L., Koay, M., Maher, M. J., Xiao, Z. & Wedd, A. G. Intermolecular Transfer of Copper Ions from the CopC Protein of Pseudomonas syringae. Crystal Structures of Fully Loaded CuICuII Forms. *J. Am. Chem. Soc.* **128,** 5834–5850 (2006).
43. Kim, S., Ståhlberg, J., Sandgren, M., Paton, R. S. & Beckham, G. T. Quantum mechanical calculations suggest that lytic polysaccharide monooxygenases use a copper-oxyl, oxygen-rebound mechanism. *Proc. Natl. Acad. Sci. USA* **111,** 149–154 (2014).
44. Kjaergaard, C. H. *et al.* Spectroscopic and computational insight into the activation of O2 by the mononuclear Cu center in polysaccharide monooxygenases. *Proc. Natl. Acad. Sci. USA* **111,** 8797–8802 (2014).
45. Makris, T. M., von Koenig, K., Schlichting, I. & Sligar, S. G. Alteration of P450 Distal Pocket Solvent Leads to Impaired Proton Delivery and Changes in Heme Geometry . *Biochemistry* **46,** 14129–14140 (2007).
46. Span, E. A. & Marletta, M. A. The framework of polysaccharide monooxygenase structure and chemistry. *Curr. Opin. Struct. Biol.* **35,** (2015).
47. Tian, C. *et al.* Systems analysis of plant cell wall degradation by the model filamentous fungus Neurospora crassa. *Proc. Natl. Acad. Sci. USA* **106,** 22157–22162 (2009).
48. Glass, N. L., Schmoll, M., Cate, J. H. D. & Coradetti, S. Plant Cell Wall Deconstruction by Ascomycete Fungi. *Annu. Rev. Microbiol.* **67,** 477–498 (2013).
49. Phillips, C. M., Iavarone, A. T. & Marletta, M. A. Quantitative Proteomic Approach for Cellulose Degradation by Neurospora crassa. *J. Proteome Res.* **10,** 4177–4185 (2011).
50. Nishiyama, Y., Langan, P. & Chanzy, H. Crystal structure and hydrogen-bonding system in cellulose Ibeta from synchrotron X-ray and neutron fiber diffraction. *J. Am. Chem. Soc.* **124,** 9074–9082 (2002).
51. Beeson, W. T., Phillips, C. M., Cate, J. H. D. & Marletta, M. A. Oxidative Cleavage of Cellulose by Fungal Copper-Dependent Polysaccharide Monooxygenases. *J. Am. Chem. Soc.* **134,** 890–892 (2012).

52. Klinman, J. P. The Copper-Enzyme Family of Dopamine b-Monooxygenase and Peptidylglycine a-Hydroxylating Monooxygenase: Resolving the Chemical Pathway for Substrate Hydroxylation. *J. Biol. Chem.* **281,** 3013–3016 (2006).
53. Denisov, I. G., Makris, T. M., Sligar, S. G. & Schlichting, I. Structure and Chemistry of Cytochrome P450. *Chem. Rev.* **105,** 2253–2278 (2005).
54. Prigge, S. T., Eipper, B. A., Mains, R. E. & Amzel, L. M. Dioxygen Binds End-On to Mononuclear Copper in a Precatalytic Enzyme Complex. *Science (80-.).* **304,** 864–867 (2004).
55. Rosenzweig, A. C. & Sazinsky, M. H. Structural insights into dioxygen-activating copper enzymes. *Curr. Opin. Struct. Biol.* **16,** 729–735 (2006).
56. Holm, R. H., Kennepohl, P. & Solomon, E. I. Structural and Functional Aspects of Metal Sites in Biology. *Chem. Rev.* **96,** 2239–2314 (1996).
57. Shook, R. L. & Borovik, A. S. Role of the secondary coordination sphere in metal-mediated dioxygen activation. *Inorg Chem* **49,** 3646–3660 (2010).
58. Olson, J. S. *et al.* The role of the distal histidine in myoglobin and haemoglobin. *Nature* **336,** 265–266 (1988).
59. Yoshioka, S. *et al.* Roles of the proximal hydrogen bonding network in cytochrome P450cam-catalyzed oxygenation. *J Am Chem Soc* **124,** 14571–14579 (2002).
60. Weiland, J. J. Rapid procedure for the extraction of DNA from fungal spores and mycelia.
61. Bardiya, N. & Shiu, P. K. Cyclosporin A-resistance based gene placement system for Neurospora crassa. *Fungal Genet Biol* **44,** 307–314 (2007).
62. Otwinowski, Z. & Minor, W. Processing of X-ray diffraction data collected in oscillation mode. *Methods Enzym.* **276,** 307–326 (1997).
63. Emsley, P. & Cowtan, K. Coot: model-building tools for molecular graphics. *Acta Crystallogr. Sect. D Biol. Crystallogr.* **60,** 2126–2132 (2004).
64. Collaborative Computational Project, N. The CCP4 suite: programs for protein crystallography. *Acta Crystallogr. Sect. D Biol. Crystallogr.* **50,** 760–763 (1994).
65. Finn, R. D. *et al.* HMMER web server: 2015 update. *Nucleic Acids Res* **43,** W30-8 (2015).
66. Kittl, R., Kracher, D., Burgstaller, D., Haltrich, D. & Ludwig, R. Production of four Neurospora crassa lytic polysaccharide monooxygenases in Pichia pastoris monitored by a fluorimetric assay. *Biotechnol. Biofuels* **5,** 79–91 (2012).
67. Persson, I., Persson, P., Sandstrom, M. & Ullstrom, A.-S. Structure of Jahn-Teller distorted solvated copper(II) ions in solution, and in solids with apparently regular octahedral coordination geometry. *J. Chem. Soc., Dalt. Trans.* 1256–1265 (2002).
68. Paithankar, K. S. & Garman, E. F. Know your dose: RADDOSE. *Acta Crystallogr D Biol Crystallogr* **66,** 381–388 (2010).
69. Tan, T. C. *et al.* Structural basis for cellobiose dehydrogenase action during oxidative cellulose degradation. *Nat Commun* **6,** 7542 (2015).
70. O'Dell, W. B., Agarwal, P. K. & Meilleur, F. Oxygen Activation at the Active Site of a Fungal Lytic Polysaccharide Monooxygenase. *Angew. Chemie, Int. Ed. English* **56,** 767–770 (2017).
71. Lee, J. Y. & Karlin, K. D. Elaboration of copper-oxygen mediated CH activation chemistry in consideration of future fuel and feedstock generation. *Curr Opin Chem Biol* **25,** 184–193 (2015).
72. Hathaway Billing, D. E., B. J. The electronic properties and stereochemistry of mono-

nuclear complexes of the copper(II) ion. *Coord. Chem. Rev.* **5,** 143–207 (1970).
73. Span, E. A., Suess, D. L. M., Deller, M. C., Britt, R. D. & Marletta, M. A. The Role of the Secondary Coordination Sphere in a Fungal Polysaccharide Monooxygenase. *ACS Chem. Biol.* **12,** (2017).
74. Bissaro, B. *et al.* Oxidative cleavage of polysaccharides by monocopper enzymes depends on H2O2. *Nat. Chem. Biol.* **13,** 1123–1128 (2017).
75. Couturier, M. *et al.* Lytic xylan oxidases from wood-decay fungi unlock biomass degradation. *Nat. Chem. Biol.* **14,** 306–310 (2018).
76. Soanes, D. M., Chakrabarti, A., Paszkiewicz, K. H., Dawe, A. L. & Talbot, N. J. Genome-wide transcriptional profiling of appressorium development by the rice blast fungus Magnaporthe oryzae. *PLoS Pathog* **8,** e1002514 (2012).
77. Maddi, A., Dettman, A., Fu, C., Seiler, S. & Free, S. J. WSC-1 and HAM-7 are MAK-1 MAP kinase pathway sensors required for cell wall integrity and hyphal fusion in Neurospora crassa. *PLoS One* **7,** e42374 (2012).
78. Leeder, A. C., Jonkers, W., Li, J. & Glass, N. L. Early colony establishment in Neurospora crassa requires a MAP kinase regulatory network. *Genetics* **195,** 883–898 (2013).
79. Glass, N. L., Rasmussen, C., Roca, M. G. & Read, N. D. Hyphal homing, fusion and mycelial interconnectedness. *Trends in Microbiology* **12,** 135–141 (2004).
80. Fu, C. *et al.* Identification and characterization of genes required for cell-to-cell fusion in Neurospora crassa. *Eukaryot Cell* **10,** 1100–1109 (2011).
81. Guindon, S. *et al.* New algorithms and methods to estimate maximum-likelihood phylogenies: Assessing the performance of PhyML 3.0. *Syst. Biol.* **59,** 307–321 (2010).
82. Read, S. M., Currie, G. & Bacic, A. Analysis of the structural heterogeneity of laminarin by electrospray-ionisation-mass spectrometry. *Carbohydr. Res.* **281,** 187–201 (1996).
83. Galagan, J. E. *et al.* The genome sequence of the filamentous fungus Neurospora crassa. *Nature* **422,** 859–868 (2003).
84. Green, K. A. *et al.* SymB and SymC, two membrane associated proteins, are required for Epichloe festucae hyphal cell-cell fusion and maintenance of a mutualistic interaction with Lolium perenne. *Mol Microbiol* **103,** 657–677 (2017).
85. Lalucque, H. *et al.* IDC2 and IDC3, two genes involved in cell non-autonomous signaling of fruiting body development in the model fungus Podospora anserina. *Dev Biol* **421,** 126–138 (2017).